# Polymer Membranes – Fractal Characteristics and Determination of Roughness Scaling Exponents

Daniel Johnson[1*] and Nidal Hilal[1,2]

1. *Centre for Water Advanced Technologies and Environmental Research (CWATER), College of Engineering, Swansea University, Swansea SA2 8PP, United Kingdom*
2. *NYUAD Water Research Center, New York University Abdu Dhabi, Abu Dhabi, United Arab Emirates*

* Corresponding author, email: d.j.johnson@swansea.ac.uk

## Abstract

Surface roughness is a parameter widely reported when characterising membrane surfaces, due to its effect on membrane properties, such as fouling / biofouling and wetting. However, a surface does not have a single roughness value, rather the magnitude of measured roughness is dependent on the length scales of measurement. Here, we report findings from roughness measurements of several commercial filtration membrane surfaces using atomic force microscopy. All membranes showed self-affine behaviour at scan sizes below approximately 10 μm, where the magnitude of root mean squared roughness, $R_q$, was described by both the scan length and an exponential factor, $H$. Furthermore, we show that values of $H$ can be obtained from power spectra of AFM images using a relatively simple approach. Using values of $H$ and $R_q$ obtained at a single scan size from image power spectra allowed us to estimate, within reasonable error, $R_q$ values at other scan size, below a cross-over length. Above this crossover length roughness scaling was linear, rather than exponential for the membranes studied.

## Keywords

Polymer membrane, roughness, atomic force microscopy, roughness scaling, surface characterization

## Highlights

- Study of effect of measurement length on roughness values for membrane surfaces
- Polymer membranes behave as self-affine surfaces described by exponential factor
- Values of $H$ calculated from power spectra of images at single scan sizes
- Estimation of roughness at various length scales using values from single scan sizes

## 1. Introduction

Polymer membranes are increasingly being used in water treatment applications [1], including production of potable water from saline sources [2, 3], treatment of domestic wastewater [4, 5], reuse and recycling of industrial wastewater [6-8] and treatment and reuse of produced water from oil extraction [9-11]. Whilst the membrane processes used in these applications have many advantages over other processes, fouling and biofouling of these membranes remains the major barrier to improved process and cost efficiency [12-14]. Fouling can take the form of inorganic scaling, particulate pore blocking, formation of cake layers on the membrane surface, and growth of bacterially derived biofilms. All of these forms of fouling serve to decrease membrane flux, leading to increased operating costs, due to higher trans-membrane pressure required to maintain the required flow rate, down-time and chemicals required for membrane cleaning and reduced membrane operating life.

~~Generally, membrane fouling can be classified as reversible or irreversible, depending on whether it is removable by simple process procedures, such as backwashing, or can only be removed by the use of chemical treatments, if at all, respectively. Alternatively, it can be considered as external (i.e. surface) or external depending on the locus of foulant material. Typically, external fouling is largely reversible. Finally, fouling can also be categorised depending on the nature of the fouling material – i.e. biofouling, organic, inorganic and colloidal fouling.~~ As roughness is a parameter describing surfaces, external fouling is of major relevance, and may be caused by any of the types of foulant material. During fouling it is possible, or even likely, that several types of fouling will occur simultaneously. Several mechanisms have been proposed for fouling growth and initiation, including adsorption of soluble compounds to the membrane surface, cake layer formation through the surface deposition of solids, and pore blocking. Biofouling involves a mixture of surface modification by dissolved substances and surface-surface interactions involving biological particles. Initial attachment of foulants and build-up of fouling layers on the membrane surface may be described by surface interactions between the foulants and surface molecules, usually described by Derjaguin-Landau-Verwey-Overbeek (DLVO) or related theories which incorporate acid-base, van der Waals and electrostatic double layer forces [15-17]; filtration based mechanisms, where permeate drag forces overcome diffusion-originating back

transport causing material to adhere to the surface / fouling layer [18-20]; and chemical potential mediated mechanisms in gel layers [21-23], where a Flory-Huggins mechanism [24] contributes to an increased specific resistance of the fouling layer. Membrane fouling has been extensively covered in the literature with a number of comprehensive reviews on the subject available [25-28].

The surface roughness of membranes, and indeed any other surface, plays a major role in modulating interactions between the surface and surrounding medium, and hence plays a major role in fouling and biofouling [29-37]. This is primarily due to roughness changing the surface area and texture available to be fouled [38], as well as affecting the water contact angle [39, 40], acid-base interactions [33] and also the surface zeta-potential [41]. The majority of studies on the effect of roughness on fouling have shown that a smoother surface tends to be less afflicted by fouling than a rougher surface due to the lower surface area available for foulant attachment. However, the relationship between roughness and fouling can be complex, and for fouling of surfaces by particulates the interplay between the size of surface peaks and troughs on the membrane and the size of particulates and their surface features can greatly affect the interaction area available [42-46]. For instance, Rabinovich et al [47] determined that even a small amount of surface roughness could decrease particle adhesion compared with a perfectly smooth surface. In addition, roughness measurement of membranes has been used to assess changes to membrane surfaces during surface modification [48-52] or fouling layer growth [53-55]. For this reason surface roughness is of great interest when characterizing membranes, particularly if those membranes are being developed to show resistance to surface fouling.

Surface roughness can be assessed by both physical and optical means. One popular technique for characterizing surfaces and quantifying their surface roughness is atomic force microscopy (AFM) ~~[56-60]~~. This technique directly visualizes the surface at high resolution, building up a topographic map of the surface, where a number of parameters, including root mean square roughness, $R_q$ and roughness average, $R_a$, can be directly measured from the height profile of the surface. For instance the $R_q$ can be calculated from the following formula [56]:

$$R_q = \sqrt{\frac{1}{mn}\sum_{i=1}^{m}\sum_{j=1}^{n} Z^2(x_i,x_j)} \quad (1)$$

where $Z_{i,j}$ is the height of an individual pixel and $m$ and $n$ are the number of pixels in the $x$ and $y$ directions. Essentially, the $R_q$ represents the standard deviation in heights of the image pixels. However, one issue with the use of these and similar parameters is that they are not scale invariant, i.e. as the size of the scan is increased the size of the measurement increases [57-60]. Within the field of membrane development, measurements usually are made at a small number of scan sizes and the values reported. This makes it difficult to compare roughness characteristics measured by different groups and in different publications if the scan ranges at which the values obtained are not identical. This is not an AFM specific problem, but is a fundamental property of roughness itself, with scaling an issue for other methods of surface roughness determination [61-64]. Clearly, parameters such as $R_q$ and $R_a$, which only contain information about surfaces obtained in the $z$-direction, when reported alone are insufficient to fully characterize membrane surface roughness or to allow comparison between reported measurements taken at different length scales. To overcome this issue additional parameters need to be reported in research publications to allow this scaling effect to be properly accounted for.

A number of commonly occurring surfaces have fractal characteristics, having a statistical self-similarity as the scale at which they are observed is altered [65, 66]. Such surfaces are described as being self-affine, and typically the scaling behaviour can be described by an exponential factor. Much of the study of such surfaces have been in the fields of crack propagation and growth of metal films, as well as some other materials. Recently it has been reported by both Zhang et al [67] and Feng et al [32] that polymer membrane surfaces with random roughness can be modelled using fractal functions. In addition, Wong et al [41] examined surface roughness of a wide variety of membranes and found that their behaviour could be described using fractal geometry, with linear growth of logarithmic plots of roughness versus scan size.

*Determination of Roughness Exponent*

It has long been noted that self-affine surfaces have roughness characteristics which scale according to a power law [68]. For a self-affine surface the relationship between $R_q$ and the length scale of measurements follows the following relationship [69, 70]:

$$R_q = a.L_0^H \tag{2}$$

where *H* is the roughness exponent (often referred to as the Hurst exponent), $L_0$ is the measurement length and *a* is an arbitrary constant.

For AFM scans, when measurements have been made across a suitably large range of scan sizes then the roughness exponent can be extracted from the slope of a plot of the natural logs of *Rq* versus $L_0$ [70] :

$$H = \frac{d\ log\ R_q}{d\log L_0} \tag{3}$$

Whilst this is easily achievable, to image several repeats at a large number of individual scan sizes can be particularly time consuming. This is likely to render derivation of the roughness exponent impractical when there are a large number of membrane samples to be examined and compared such as during membrane development.

*H* is closely connected to the fractal dimension, $D_f$ [65, 71]:

$$H = D - D_f \tag{4}$$

where *n* = 3 for a surface (i.e. $2<D_f>3$) [63] and 2 for a time series etc., such as a PSD plot ($1<D_f>2$) [72]. From the power spectral density plot of an AFM image the following equation may be fitted to the linear part of the power curve, allowing the derivation of the fractal dimension of the surface [69]:

$$D_f = \frac{5}{2} + \frac{1}{2}\frac{d\log p(f)}{d\log f} \tag{5}$$

where *p(f)* is the power spectrum of the surface profile and *f* the spatial frequency, or wavenumber. The roughness exponent can then be obtained from the fractal dimension using equation 4. According to Milman et al, significant errors may be present in the power spectrum due to statistical fluctuations, so analysis of the integrated power spectrum, *P(f)* [69] can yield a value of the fractal dimension which may be less prone to noise induced error, where the integrated power spectrum is:

$$P(f) = \int_{f}^{\infty} p(f).df \quad (6)$$

By fitting the following relationship to the integrated power spectrum, for frequencies higher than the inverse correlation length, the fractal dimension can be obtained [69, 73, 74]:

$$D_f = 2 + \frac{1}{2}\frac{d\log P(f)}{d\log f} \quad (7)$$

Other methods exist which can determine the fractal dimension of a surface, and hence *H*, including cube or box-counting, the area-perimeter method and the divider method. However, Schmittbuhl et al compared a large number of different methods to determine *H* from simulated surfaces with known values of *H*, and found that calculation of *H* from power spectra are the most reliable, generating smaller calculation derived errors [75]. Previous researchers have used cube-counting methods to determine fractal dimension of surfaces [41, 76]. However, our previous experience using cube counting was not very satisfactory [57], with fractal dimensions showing unacceptable variation at different scan sizes.

In this work we report investigations into the surface roughness of several unmodified commercially available membranes to determine and compare the roughness exponent and $R_q$ values obtained both from the natural log plot of $R_q$ versus $L_0$ as well as from the power spectra of individual height images. ~~A~~ The primary aim was to investigate whether values of *H* derived from the power spectrum of individual topographic scans taken at a single scan size would allow accurate prediction of $R_q$ values at other scan sizes. *H* values were calculated using both non-integrated (equation 5) and integrated power spectra (equation 7). This was because little extra effort was needed in calculating both than either singly, and to provide a comparison of which method would allow a more reliable calculation of *H*.

## 2. Materials and Methods

All measurements were carried out using a Multimode AFM with Nanoscope IIIa controller (Bruker) using manufacturer supplied software. All measurements were made using tapping mode in air with RTESPA tapping mode probes (Bruker), with a nominal imaging tip radius of curvature of 8 nm, nominal resonant frequency 300 kHz and nominal spring constant of 40 N

$m^{-1}$. All probes were cleaned in a plasma asher system using laboratory air to remove organic contaminants prior to use (Femto Plasma System, Diener Electronics, Germany). All images were obtained as 1 Hz scan rates, except for 80 μm scans where the scan rate was adjusted to 0.5 Hz. Images were continuously monitored for quality, with feedback parameters and amplitude set-point adjusted to optimise surface tracking, whilst minimising noise. Tapping frequency was set at 5% below the resonant frequency of the cantilever, as determined during cantilever tuning. Images were carefully inspected for artefacts showing blunted or otherwise damaged tips, with tips immediately replaced if such artefacts occurred.

Accuracy of information obtained in the *z*-direction is crucial for roughness measurements [77]. To ensure accuracy of data obtained, the instrument *z*-movement was calibrated prior to experiments by scanning on a calibration standard (VGRP-15M, Bruker AXS) containing regular pits of known depth (180 nm). Instrument parameters were then adjusted so that measured parameters were identical to known values for the calibration grid. The same calibration grid was used to calibrate *x*, *y* distances and image *x*,*y* orthogonality. Fast fourier transforms (FFTs) of images were examined in instrument software. The radial symmetry of FFTs allows determination of the extent to which a surface is isotropic, as suggested by Jacobs et al [78].

Commercially available polymer membranes were used in this study. Three were nanofiltration membranes: Filmtech type NF270, NF90 (Dow Corning) and Spiratech TFC-SR3 (Koch); and one was a reverse osmosis membrane: Filmtech BW30 (Dow Corning). All four membranes were of a thin film composite structure with a polyamide active layer. Measurements were made on membranes as supplied by the manufacturer, with no surface preparation undertaken apart from immobilisation on a metal sample disk using double sided adhesive tape. Commercial membranes when received in their dry state typically contain substances intended to preserve their structure, which are washed out during filtration and subsequent drying will lead to pore collapse. As a ~~result~~result, it was decided to take the membranes as supplied without prior flushing with water.

Measurements were carried out at 10 different locations on each membrane surface, selected arbitrarily. For measurements on each membrane area a 1 x 1 μm scan was carried out first and then the scan size was ramped up sequentially in the order 1, 2, 5, 10, 20, 40 and 80 μm. For each locus the full range of imaging sizes were obtained, beginning at the smallest scan

size (1 µm) and sequentially increasing until the maximum scan size (80 µm) had been recorded. This was to ensure that as much of the area scanned as possible was pristine, minimizing any potential effects of wear on the surface due to repeated scans. Captured data was processed using the Nanoscope Analysis 1.8 offline analysis software (Bruker). All images were corrected using a 2nd order flattening function to remove offset and sample tilt before any further analysis was carried out. Image power spectral density (PSD) was obtained using a 2D isotropic computation and the data was exported in text files for curve fitting in Excel.

Power spectra for each height image were obtained using the instrument software and computed as 2D isotropic spectra using instrument software. Linear fits to the power spectra of each individual image were made and equation 5 used to calculate the fractal dimension, $D_f$, from the slope, allowing the roughness exponent, $H_a$, to be obtained using equation 4. Integrated power spectra, $P(f)$, (equation 6) were also plotted and linear fits were made to obtain the slope. Fits were made to the portion of the data at frequencies higher than the inverse of the correlation length for each image, as determined by the instrument software. Equation 7 was then used to calculate values of $D_f$ from the slope, which were then used to calculate roughness exponent values, $H_b$ using equation 4.

From the values of $H_a$ and $H_b$ calculated from the power spectra at individual scan sizes it was possible to estimate $R_q$ values for other scan sizes. This was done by estimating values of $a$ from $R_q$, $H$ and $L_0$ values for a discrete scan length and then using equation 2 to generate $R_q$ values for other scan lengths. This was carried out using data obtained from scan sizes of 10 µm and below only.

## 3. Results and Discussion

### *3.1 AFM measurements of $R_q$*

A representative set of AFM topographic images are shown in figures 1-4 for the NF270, BW30, NF90 and TFC membranes respectively. Each series of images shown were taken from the same scanning locus for each particular membrane sample. ~~The root mean squared surface roughness ($R_q$) was obtained from all images after images had first been processed to~~

~~remove sample surface offset and tilt.~~ As can be seen, ~~features of successively larger size are revealed with increasing scan size~~at small scan sizes images show nano-scale structure of the membranes, whilst at larger scan sizes membrane defects such as ridges and holes. Mean values of $R_q$ plotted versus scan length are shown in figure 5 for each membrane. ~~[57, 58][79, 80][36][36][36, 81][80][79]Literature values for these membranes show a broadly similar trend with NF90 and BW30 membranes being much rougher as scan sizes of 1 to 10 μm, and with the Koch TFC-SR3 membrane being by far the smoothest [36, 57, 58, 80-82]. Differences in the absolute values may be due to variations between batches and selection of membrane areas for imaging. In this study 10 replicates were made at each scan size for each membrane, so we are confident that the values we have obtained are reliable for our membrane samples.~~

For all membranes $R_q$ values increase as scan size is increased, as would be expected. For all membranes the increase initially has a curved profile, which appears to ~~becomes linear~~change approximately from the 20 μm scan size and above. Whilst the smallest scan sizes show nodules constituting the upper layer nanostructure of the membrane, larger scan sizes demonstrate ~~meso-scale~~ defects in the membrane surface, likely resulting from artefacts of membrane production and damage, including ridges, grooves and pits. These features are likely to be the cause of the large variation in measurement values at large scan sizes, as demonstrated by the larger standard deviation shown by the error bars in fig. 5. It is difficult to determine conclusively which of these features can be attributed to manufacturing defects and which had arisen subsequently through handling or contamination. Many of the defects are grooves or pits, so are not contamination. Whilst the grooves could have been caused by damage due to rolling of the membranes, it is worth noting that the BW30 samples were received as flat samples which had not been rolled, and also contained these features. Another type of feature seen are ridges on the membrane surface. The ridges visible in the example images for NF270 (figure 1) are apparent from the smallest to largest scan size. At larger scan sizes they take on the appearance of drying marks. As these ridges here seem to have the same size and shape as basic structural units of the rest of the membrane (visible at small scan sizes) and ~~that~~ we had not exposed these membranes to fluid, it is likely that these are a result of the manufacturing process. Other raised features, such as seen in Fig 4 e and f, are difficult to differentiate between surface contamination and membrane surface defects.

It is worth noting that such features were unavoidable at large scan sizes. During first approach the probe tip was positioned over a pristine area of the membrane surface, as seen through the instrument optical microscope. However, such features were so prevalent that they were for practical purposes unavoidable at large scan sizes. Such features were previously remarked on for NF270 and BW30 membranes in a study by Allen et al [36] of topographical heterogeneities. It was found that such features were disproportionally populated by bacterial cells during biofouling tests, and as such are likely to play an important role in biofilm growth.

Values of *Rq* obtained from the literature are shown in table 1 for comparison with the measurements made here. For membrane NF270 values are broadly similar to the ones ~~obtained here~~we report. At 1 μm scan sizes literature values range between about 2.5 to 4.9 [57, 58]; 3.4 to 8.6 at 2μm [79, 80] and 23.7 at 10 μm [36]. The mean values obtained in this work fit within these ranges at the smaller scan sizes, but is below the value recorded by Allen et al [36]. For BW30, values have been recorded as 53.9 and 75.0 nm for 10 and 20 micron scans [36, 81], with values from this work of 80.5 and 88.0 respectively. For NF90 values have been recorded at 22.8 nm [80] and 76.8 nm [79], for 2μm scan sizes, compared with 2μm here. Interestingly, Carvalho reports roughness values for NF90 membrane at a range of scan lengths, with a similar *Rq* vs $L_0$ curve [82]. Finally, for the TFC-SR3 membrane, Gautam reported an *Rq* value of 8.0 at 20 μm, compared with 4.8 μm here. Literature values for these membranes show a broadly similar trend with NF90 and BW30 membranes being much rougher as scan sizes of 1 to 10 μm, and with the Koch TFC-SR3 membrane being by far the smoothest [36, 57, 58, 80, 81, 83]. Differences in the absolute values may be due to variations between batches and selection of membrane areas for imaging, as well as to how the membranes have been treated prior to imaging. For instance, if membranes are imaged subsequent to imaging in air, washing out of preservatives and then drying are likely to lead to a collapse of the membrane structure. In addition changes in adhesive or long-range interaction or other forces due to the presence or absence of membrane preservatives, may modify the tip-sample interaction forces, which can affect the image resolution of a soft sample [84].

Figure 6 shows the plot of the natural logarithms of $R_q$ and $L_0$ for the same data. For the NF270 and TFC-SR3 membranes, ~~As can be seen from comparing the two plots,~~ $R_q$ increases along with an increase of $L_0$, with two different slopes depending upon the scan size for all membranes, which both show a clear increase in the slope gradient at scan sizes above a cross-over length. For the NF90 and BW30 membranes the change in slope was much less pronounced, with a decreased gradient seen at scan lengths above the cross-over. ~~H values~~Gradients for the two slopes in each curve, along with the cross-over length were calculated using linear regression of the $\log_e R_q$ versus $\log_e L_0$ data. This information is summarised in table 2~~1~~. Confidence intervals were calculated for each gradient, with an assumed confidence level of 98%. From table 2 it can be seen that there is no overlap between the upper and lower intervals for NF270 and TFC-SR3, suggesting that there is a significant change in gradient. For the NF90 and BW30 gradients however, the intervals have a significant overlap, meaning the existence of a crossover is not well supported.~~ There appears to be no correlation between *H* and crossover length.~~

~~The change in slope is most marked for NF270 and TFC-SR3 membranes, which both show a clear increase in the slope gradient at scan sizes above a cross-over length. For the NF90 and BW30 membranes the change in slope was much less pronounced, with a decreased gradient seen at scan lengths above the cross-over.~~ Indeed for these two membranes, particularly BW30, a single linear fit to the whole of the data would suffice almost as well as the individual fits to the upper and lower portions of the curve. ~~This also makes determination of the crossover length much less certain for these two membranes, as it is less clear which points would be best fitted by the upper and lower fits.~~ For these two membranes, if ~~treated as having no clear crossover~~assuming a single gradient, then ~~H values~~gradients are obtained of 0.29 and 0.38 for the BW30 and NF90 membranes respectively. It is worth noting that $R_q$ values for the NF270 and TFC membranes are generally much lower than for the NF90 and BW30 membranes at all scan sizes, but particularly at low $L_0$ values.

Previously Wong et al [41] reported roughness values for a number of membranes across several orders of magnitude, but only saw a single scaling regime for each membrane. This difference could be material specific. The membranes investigated by Wong et al were all either poly ether sulfone (PES) or poly vinyl pyrrolidone (PVDF), whereas the membranes investigated here all have a polyamide active surface. Multi-scaling regimes have however

been observed ~~previously~~for other materials. For instance, Lapique et al [85] when ~~observing~~ studying roughness scaling of polymer fracture surfaces observed a single scaling regime with homopolymers, but saw a crossover to a second scaling regime at longer length scales when examining copolymers. Furthermore, the cross-over length corresponded to the average distance between polyethylene and polypropylene particles. This is similar to our observations, where a second scaling regime may be observed at scan sizes large enough to pick up ~~meso and micro-scale~~relatively large defects.

~~The change in slope is most marked for NF270 and TFC-SR3 membranes, which both show a clear increase in the slope gradient at scan sizes above a cross-over length. For the NF90 and BW30 membranes the change in slope was much less pronounced, with a decreased gradient seen at scan lengths above the cross-over. Indeed for these two membranes, particularly BW30, a single linear fit to the whole of the data would suffice almost as well as the individual fits to the upper and lower portions of the curve. This also makes determination of the crossover length much less certain for these two membranes, as it is less clear which points would be best fitted by the upper and lower fits. For these two membranes, if treated as having no clear crossover, then $H$ values are obtained of 0.29 and 0.38 for the BW30 and NF90 membranes respectively. It is worth noting that $R_q$ values for the NF270 and TFC membranes are generally much lower than for the NF90 and BW30 membranes at all scan sizes, but particularly at low $L_0$ values.~~

It has been reported previously that surfaces may typically show self-affine behaviour below a characteristic correlation length, but show non-self-affine behaviour due to saturation at sizes above this correlation length. For the self-affine part of the data, scaling is dominated by the roughness exponent, $H$, whilst at larger measurement sizes it increases by a constant factor based on the $R_q$ [61]. ~~For our data (figure 5) it can be seen that for all membranes the shape of the $R_q$ versus $L_0$ curve switches from a typical exponential shape below the 10 µm measurement to a linear relationship above this value. This approximates to the cross-over length values predicted from the log-log plots (figure 6) which are between 4.46 and 7.17 µm.~~ It is likely, at least in terms of the membranes examined here, that at smaller scan sizes the roughness is dominated by the nano-scale structures formed by the membrane material, but above this is dominated by the presence of macroscale structures, including large wavelength undulations and surface defects. ~~Interestingly, the two membranes which show the lowest~~

~~difference in *H* for the lower and upper sections are~~ BW30 and NF90~~, which~~ have a much more pronounced surface roughness at $L_0$ = 1 to 10 μm than the other membranes. This increased roughness ~~due to~~of the nano-scale structures may mean that the macroscale structures observed with larger scan sizes contribute less to the measured $R_q$ than for the smoother NF270 and TFC membranes. An alternative explanation may be that the scaling regime has transferred from a local to a global regime for the NF270 and TFC-SR3 membranes~~, as suggested previously by Mandelbrot~~ [72].

*3.2 Calculation of H from AFM Power Spectra*

Representative linear fits to power spectra and integrated power spectra (from an image obtained from sample NF270) are shown in figures 7a and 7b respectively. As can been seen from figure 7b, the data is highly non-linear, with a linear slope, as needed for equation 7, merely giving the average slope for the portion of the curve above the inverse correlation length. In practise using values above this point only excluded the initial few points, making little difference to the curve fitting.

~~Power spectra for each height image were obtained using the instrument software and computed as 2D isotropic spectra using instrument software. Linear fits to the power spectra of each individual image were made and equation 5 used to calculate the fractal dimension, $D_f$, from the slope, allowing the roughness exponent, $H_a$, to be obtained using equation 4. A representative power spectrum (from sample NF270) with dotted line representing a linear fit is shown in figure 7a.~~

~~Integrated power spectra, *P(f)*, (equation 6) were also plotted and linear fits were made to obtain the slope. Equation 7 was then used to calculate values of $D_f$ from the slope, which were then used to calculate roughness exponent values, $H_b$ using equation 4. A representative linear fit to a single integrated power spectrum is shown in figure 7b.~~

Mean $D_f$ values calculated using both methods, along with standard deviation values, are tabulated in supplementary table S1. Values of $D_f$ are with-in the range $1 < D_f > 2$ as would be expected from a 2D profile [86], with minimum and maximum values of 1.423 and 1.849 respectively. This compares with a value of 1.506 reported by Zhang et al for a PVDF surface

from 5 μm AFM scans using a Weierstrauss- Mandelbrot function [67]. In the case of the Zhang et al experiments, 5 discrete line profiles were taken from each image and power spectra derived from the line scans were used to calculate $D_f$. For the approach used here, the software progressively samples the surface of the 2D FFT image at a range of sampling frequencies [87], hence deriving the power spectra from the whole image rather than discrete user selected horizontal scans.

Mean values for $H_a$ and $H_b$ versus scan size are shown in figure 8. Values for both $H_a$ and $H_b$ are similar in magnitude to $H$ derived from the natural log plots of the $R_q$ versus $L_0$, although variation does seem to be slightly less for $H_a$ than for $H_b$. On average, values of $H_b$ tend to be slightly higher than those for $H_a$, although the difference in most cases is not large.

It is of note that the values of $H_a$ and $H_b$ do not remain constant, particularly when comparing those values obtained at small scan sizes. This could be due to effects of sampling. At small scan sizes the sizes of image pixels are typically lower than the expected resolution of the instrument, which is essentially set by the interaction area between the probe tip and the sample (based on the radius of curvature of the probe and the sample $R_q$). Klapetek et al [88] demonstrated using a simulated surface that the finite dimensions of the AFM probe tip tend to misrepresent the precise fractal nature of the surface. Images here were obtained with a pixel resolution of 512 x 512, meaning that for a 1 μm scan an image pixel would be expected to be on the order of 2 nm across, compared with a probe nominal radius of curvature quoted by the manufacturer of approximately 8 nm. This means that adjacent pixels at small scan sizes will effectively contain the same information, leading to smaller effective sampling rates. In fact, it is possible to derive a reliability cut-off for AFM measurements, where frequencies above this number in the PSD give no meaningful information [78] – for small scan sizes this portion of the PSD is likely to be proportionately larger. This may mean that the $H$ values obtained at the lowest scan sizes are necessarily less reliable.

In addition, changes in $H$ as scan size increases are not identical for $H_a$ and $H_b$. For instance, for BW30 and NF90, $H_a$ values increase, up to 10 μm, then steadily decrease, whereas NF270 steadily decreases and the TFC-SR3 membrane stay broadly the same. This behaviour seems to be membrane specific. However, for $H_b$ values there is no clear initial trend, but above 10 μm the values for all the seem to converge, to approximately similar values between 0.357 and 0.387 for the 80 μm scans, which is also reflected in much smaller standard deviations at

large scan sizes. This suggests a much higher reproducibility in $H_b$ values seen at greater scan sizes, which does not occur for values derived from the non-integrated power spectra.

Zahn and Zösch ~~did find~~found that the measured fractal dimension decreased as scanning speed was increased, which would lead to an increase in $H$ [89]. In our experiments the scan rate was kept constant from 1 to 40 μm, so this effect could account for some of the variation seen. However, Zahn and Zösch only examined effect of imaging speed at a single scan size and the change in $H_a$ and $H_b$ we observed was generally a monotonic increase, so it is not clear the effect of this change of scanning speed with scan length progression. However, to maintain the scan speed at a constant value whilst varying the scan rate and scan length over orders of magnitude would not have been practicable, as large scan sizes maintained at the same speed as for the 1 μm scans (e.g.1 μm $s^{-1}$), would lead to prohibitively long acquisition times and images would be prone to distortions due to drifting. Conversely, applying fast scanning speeds to small scan sizes would have risked poor surface tracking. Maintaining scan rate, rather than scan speed allowed for better image optimisation.

~~In addition it~~It has been ~~was~~ pointed out by Schmittbuhl et all that when determining $H$ from power spectra at smaller sampling sizes errors tend to be greater [75]. This may explain the variation of $H_a$ and $H_b$ seen calculated from the lowest scan sizes.

~~It is also interesting to note that~~ Aalthough there is a marked change in roughness scaling~~, above the cross-over length~~ for the NF270 and TFC-SR3 membranes~~, noted from figures 5 and 6,~~ values of $H$ derived from the power spectra remain broadly similar at values throughout the range of scan sizes examined~~, both above and below the crossover length~~. ~~This is especially apparent when comparing $H_a$ and $H_b$ values with the upper value of slope (Table 1) seen for the NF270 and TFC-SR3 membranes.~~ This again suggests that roughness increases above the cross-over length were due to the contribution of ~~meso-scale~~ defects, which may not show a fractal or self-affine character. As a result, values of $H$ derived from AFM image power spectra may be largely probing the polymer membrane nanostructure, even at larger scan sizes.

*3.3 Estimation of $R_q$ for other scan sizes from H values calculated at single scan sizes*

~~From the values of $H_a$ and $H_b$ calculated from the power spectra at individual scan sizes it was possible to estimate $R_q$ values for other scan sizes. This was done by estimating values of $a$ from $R_q$, $H$ and $L_0$ values for a discrete scan length and then using equation 2 to generate $R_q$ values for other scan lengths. This was carried out using data obtained from scan sizes of 10 μm and below only. Calculated~~ Values of $R_q$ ~~values~~ calculated from $H_a$ and $H_b$, ~~,~~ alongside measured $R_q$, ~~were compared with the values shown~~are compared in figure~~s~~ 9. Due to the large discrepancy between the slopes for membranes NF270 and TFC-SR3 and $H_a$, $H_b$ at larger scan sizes it was decided to restrict these calculations to ~~the lower end of the scale~~information taken at scan lengths of ≤ 10 μm.

For the majority of cases, at scan lengths of 10 μm and below the calculated $R_q$ value fit well to experimentally derived $R_q$ values. In general, closest matches between calculated and experimental values are found where the scan lengths are similar. For scan sizes of 20 μm and greater, calculated $R_q$ match poorly to measured $R_q$ values for all membranes, but was particularly marked for those with a greater difference in scaling between upper and lower scan sizes (NF270 and TFC-SR3). However, there is still a substantial deviation between measured $R_q$ and calculated $R_q$ for the NF90 and BW30 membranes above this range. ~~This suggests our interpretation that the scaling is different for these membranes at scan lengths above and below approx. 10 μm is correct.~~ One clear exception at lower scan sizes is for $R_q$ values calculated for the TFC-SR3 membrane, where significant deviation is seen from experimental and calculated $R_q$ values for 10 μm and above, as well as for $Rq$ values calculated from the 10 μm scans at all other sizes. This is not surprising when consideration is given to figure 7d and the cross-over length of 6.29 μm for this particular membrane. Whilst BW30 had a smaller calculated cross-over length, it did not have a clear transition between small and large scans, unlike in the case of the Koch TFC membrane.

~~Whilst for the membranes examined here, the calculated $R_q$ deviates at large scans sizes from measured $R_q$, it is uncertain whether this holds true for all membrane materials. Previous researchers examining other membrane materials found no cross-over for PVDF and PES membranes, suggesting that these materials have a single scaling regime [41].~~

Percentage error values were calculated to compare calculated $R_q$ with directly measured $R_q$. These are ~~summarised in figure 10, with all values~~ tabulated in supplementary information tables S4 and S5. In all cases, calculated $R_q$ values show unacceptably large error values at scan sizes of 20 μm and above.

With the exception for the case of values calculated from 10μm data with TFC-SR3 membranes, error values calculated at scan sizes of 10 μm and less, error was much lower. Generally, error at <10 μm is lower for $H_a$ values than for $H_b$, with all values showing less than 20% error, and most below 10%. In the case of values calculated for BW30 from 10 μm data error is slightly higher for $H_a$ than for $H_b$. Conversely, for the NF90 membrane calculated $R_q$ values for low scan sizes are unacceptably high (>20%). Generally, values of error are lowest when calculated for similar scan sizes, with error increasing with the greater discrepancy between the scan size used to generate the calculation and the scan size for which an Rq value was calculated. Overall, given the variable $H_a$ and $H_b$ values seen at lowest scan sizes, the poor reproducibility at large (>10 μm) scan sizes, that for values of 10μm and less, data generated at 5μm using the non-integrated power spectra (i.e. $H_a$) seems to be optimal~~, from the data seen here~~. However, there is still greater error and more variation than is desirable, so future work must focus on finding the sources of error and reducing them accordingly.

As the ten repeats for each scan size taken here is more than is normally reported in the literature, some thought needs to be given to the effect of number of scans made on the results. Figure 10 shows Ha and Hb values obtained for each scan size for membrane NF270 as the number of measurements is increased. As can be seen for Ha (figure 10a), with the exception of the 80 μm data, relatively consistent values of are obtained after averaging over 5 scans. For the 80 μm scan, the values are constantly increasing with cumulative scan number, reaching a plateau after 8 scans. With Hb values (figure 10b), a much smaller spread is seen between the scan lengths than for Ha values. In addition, again with the exception of 80 μm scans, H values become reasonably stable after approximately 3 or more averaged scans.

In general, it would seem that values of $H$ and $R_q$ obtained from integrated power spectra are more reliable, due to superior consistency, and particularly for scan sizes of 5 and 10 μm. We would recommend caution in making these calculations at scan sizes much greater than 10 μm due to the presence of surface defects commonly seen on membranes when larger

scanning areas are examined, and not at scan sizes less than 5 μm due to variation in H obtained at these scan lengths. We would also recommend a minimum of average results from scans at 3 different loci if using integrated spectra and 5 if calculating H from non-integrated spectra.

## 4. Conclusions

An examination of the effect of scan size on measured surface roughness was carried out for several commercially available polymer membranes. It was found that in all cases below a characteristic length all membranes showed self-affine behaviour, where the root means squared roughness was proportional to the scan size raised to a roughness exponent, *H*. This is behaviour has been previously reported for thin films and fracture surfaces, but has not been thoroughly explored for polymer membrane surfaces. However, above this crossover length, roughness increased linearly with scan size, possibly due to the non-self-affine contributions of ~~meso-scale and macroscopic~~larger scale membrane features, including defects, grooves etc.

Using theory describing the fractal geometry of surfaces, we extracted values of *H* from power spectra of individual AFM images. We have successfully demonstrated that this allows an estimation of the root mean squared roughness obtained at other scan sizes, within the self-affine regime. These values approximated reasonably well to experimentally observed values for those other scan sizes for scan ranges up to the cross-over length. Above this crossover length values of *H* obtained from power spectra were not able to accurately predict surface roughness.

In the literature describing the development and characterisation of membrane surfaces, AFM imaging on scales of 10 μm and below is often used to characterise surface morphology, particularly by describing various roughness parameters. Surface roughness is a primary factor in determining the likely fouling behaviour of a membrane, as well as being related to other important surface properties of membranes, such as their wetting behaviour. However, measured values depend greatly upon scan size, and in the absence of a standardised approach to membrane imaging, c~~. C~~omparison of results between different reports where different scan sizes have been used makes comparison of surface roughness impossible. The

finding here that polymer membrane roughness scales by an exponential factor that can be easily obtained from the power spectra of AFM images provides a potential solution. Whilst *H* in itself does not describe the roughness of a surface in itself [90], combined with the $R_q$ value and scan size, it allows a fair estimation of surface roughness at other length scales. As a result, we propose that reporting of *H* values alongside $R_q$ and scan size in future works would be of great utility for future investigations of surface roughness, particularly for investigations of the effect of roughness on membrane fouling. From the results here, we would also recommend obtaining *H* from the integrated power spectra of AFM surface scans at scan lengths of 5 – 10 µm, providing membrane defects are not in the images, with data from a minimum of 3 independent scans.

## 5. Acknowledgements

The authors would like to thank the Royal Society for funding this work through a Royal Society International Collaboration Award (IC160133).

## 6. References


[1] R.W. Baker, Membrane Technology and Applications, John Wiley & Sons, Incorporated, New York, UNITED KINGDOM, 2012.
[2] P.S. Goh, A.F. Ismail, N. Hilal, Nano-enabled membranes technology: Sustainable and revolutionary solutions for membrane desalination?, Desalination, 380 (2016) 100-104.
[3] E. Drioli, A. Criscuoli, E. Curcio, Integrated membrane operations for seawater desalination, Desalination, 147 (2002) 77-81.
[4] A.L. Smith, S.J. Skerlos, L. Raskin, Psychrophilic anaerobic membrane bioreactor treatment of domestic wastewater, Water research, 47 (2013) 1655-1665.
[5] T. Ueda, K. Hata, Y. Kikuoka, Treatment of domestic sewage from rural settlements by a membrane bioreactor, Water Science and Technology, 34 (1996) 189.
[6] A. Wahab Mohammad, R. Othaman, N. Hilal, Potential use of nanofiltration membranes in treatment of industrial wastewater from Ni-P electroless plating, Desalination, 168 (2004) 241-252.
[7] H.A. Qdais, H. Moussa, Removal of heavy metals from wastewater by membrane processes: a comparative study, Desalination, 164 (2004) 105-110.
[8] V.P. C., B. Roberto, V. Willy, Review: Treatment and reuse of wastewater from the textile wet-processing industry: Review of emerging technologies, Journal of Chemical Technology & Biotechnology, 72 (1998) 289-302.
[9] A. Fakhru'l-Razi, A. Pendashteh, L.C. Abdullah, D.R.A. Biak, S.S. Madaeni, Z.Z. Abidin, Review of technologies for oil and gas produced water treatment, Journal of Hazardous Materials, 170 (2009) 530-551.
[10] S. Mondal, S.R. Wickramasinghe, Produced water treatment by nanofiltration and reverse osmosis membranes, Journal of Membrane Science, 322 (2008) 162-170.
[11] M. Çakmakce, N. Kayaalp, I. Koyuncu, Desalination of produced water from oil production fields by membrane processes, Desalination, 222 (2008) 176-186.
[12] M.A. Shannon, P.W. Bohn, M. Elimelech, J.G. Georgiadis, B.J. Mariñas, A.M. Mayes, Science and technology for water purification in the coming decades, Nature, 452 (2008) 301.
[13] W.-J. Lau, A.F. Ismail, Polymeric nanofiltration membranes for textile dye wastewater treatment: Preparation, performance evaluation, transport modelling, and fouling control — a review, Desalination, 245 (2009) 321-348.
[14] M.F.A. Goosen, S.S. Sablani, H. Al-Hinai, S. Al-Obeidani, R. Al-Belushi, D. Jackson, Fouling of Reverse Osmosis and Ultrafiltration Membranes: A Critical Review, Separation Science and Technology, 39 (2005) 2261-2297.
[15] X. Cai, M. Zhang, L. Yang, H. Lin, X. Wu, Y. He, L. Shen, Quantification of interfacial interactions between a rough sludge floc and membrane surface in a membrane bioreactor, Journal of Colloid and Interface Science, 490 (2017) 710-718.
[16] X. Qu, X. Cai, M. Zhang, H. Lin, Z. Leihong, B.-Q. Liao, A facile method for simulating randomly rough membrane surface associated with interface behaviors, Applied Surface Science, 427 (2018) 915-921.
[17] J. Chen, H. Lin, L. Shen, Y. He, M. Zhang, B.-Q. Liao, Realization of quantifying interfacial interactions between a randomly rough membrane surface and a foulant particle, Bioresource Technology, 226 (2017) 220-228.
[18] M. Xie, J. Lee, L.D. Nghiem, M. Elimelech, Role of pressure in organic fouling in forward osmosis and reverse osmosis, Journal of Membrane Science, 493 (2015) 748-754.
[19] Y. Kim, S. Lee, H.K. Shon, S. Hong, Organic fouling mechanisms in forward osmosis membrane process under elevated feed and draw solution temperatures, Desalination, 355 (2015) 169-177.
[20] L.-g. Shen, Q. Lei, J.-R. Chen, H.-C. Hong, Y.-M. He, H.-J. Lin, Membrane fouling in a submerged membrane bioreactor: impacts of floc size, Chemical Engineering Journal, 269 (2015) 328-334.

[21] M. Zhang, H. Hong, H. Lin, L. Shen, H. Yu, G. Ma, J. Chen, B.-Q. Liao, Mechanistic insights into alginate fouling caused by calcium ions based on terahertz time-domain spectra analyses and DFT calculations, Water research, 129 (2018) 337-346.
[22] M. Zhang, H. Lin, L. Shen, B.-Q. Liao, X. Wu, R. Li, Effect of calcium ions on fouling properties of alginate solution and its mechanisms, Journal of Membrane Science, 525 (2017) 320-329.
[23] J. Chen, M. Zhang, F. Li, L. Qian, H. Lin, L. Yang, X. Wu, X. Zhou, Y. He, B.-Q. Liao, Membrane fouling in a membrane bioreactor: high filtration resistance of gel layer and its underlying mechanism, Water research, 102 (2016) 82-89.
[24] C.A. Finch, Chemistry and technology of water-soluble polymers, Springer Science & Business Media, 2013.
[25] H. Lin, W. Peng, M. Zhang, J. Chen, H. Hong, Y. Zhang, A review on anaerobic membrane bioreactors: Applications, membrane fouling and future perspectives, Desalination, 314 (2013) 169-188.
[26] V. Kochkodan, N. Hilal, A comprehensive review on surface modified polymer membranes for biofouling mitigation, Desalination, 356 (2015) 187-207.
[27] Q. She, R. Wang, A.G. Fane, C.Y. Tang, Membrane fouling in osmotically driven membrane processes: A review, Journal of Membrane Science, 499 (2016) 201-233.
[28] S. Jiang, Y. Li, B.P. Ladewig, A review of reverse osmosis membrane fouling and control strategies, Science of The Total Environment, 595 (2017) 567-583.
[29] E. Guillen-Burrieza, R. Thomas, B. Mansoor, D. Johnson, N. Hilal, H. Arafat, Effect of dry-out on the fouling of PVDF and PTFE membranes under conditions simulating intermittent seawater membrane distillation (SWMD), Journal of Membrane Science, 438 (2013) 126-139.
[30] K. Al-Anezi, D.J. Johnson, N. Hilal, An atomic force microscope study of calcium carbonate adhesion to desalination process equipment: effect of anti-scale agent, Desalination, 220 (2008) 359-370.
[31] N. Hilal, H. Al-Zoubi, N. Darwish, A. Mohamma, M.A. Arabi, A comprehensive review of nanofiltration membranes: treatment, pretreatment, modelling, and atomic force microscopy, Desalination, 170 (2004) 281-308.
[32] S. Feng, G. Yu, X. Cai, M. Eulade, H. Lin, J. Chen, Y. Liu, B.-Q. Liao, Effects of fractal roughness of membrane surfaces on interfacial interactions associated with membrane fouling in a membrane bioreactor, Bioresource Technology, 244 (2017) 560-568.
[33] E.M. Vrijenhoek, S. Hong, M. Elimelech, Influence of membrane surface properties on initial rate of colloidal fouling of reverse osmosis and nanofiltration membranes, Journal of Membrane Science, 188 (2001) 115-128.
[34] M. Elimelech, Z. Xiaohua, A.E. Childress, H. Seungkwan, Role of membrane surface morphology in colloidal fouling of cellulose acetate and composite aromatic polyamide reverse osmosis membranes, Journal of Membrane Science, 127 (1997) 101-109.
[35] E.M.V. Hoek, S. Bhattacharjee, M. Elimelech, Effect of Membrane Surface Roughness on Colloid−Membrane DLVO Interactions, Langmuir, 19 (2003) 4836-4847.
[36] A. Allen, A.J.C. Semião, O. Habimana, R. Heffernan, A. Safari, E. Casey, Nanofiltration and reverse osmosis surface topographical heterogeneities: Do they matter for initial bacterial adhesion?, Journal of Membrane Science, 486 (2015) 10-20.
[37] D. Johnson, F. Galiano, S.A. Deowan, J. Hoinkis, A. Figoli, N. Hilal, Adhesion forces between humic acid functionalized colloidal probes and polymer membranes to assess fouling potential, Journal of Membrane Science, 484 (2015) 35-46.
[38] P. Kaner, D.J. Johnson, E. Seker, N. Hilal, S.A. Altinkaya, Layer-by-layer surface modification of polyethersulfone membranes using polyelectrolytes and AgCl/TiO2 xerogels, Journal of Membrane Science, 493 (2015) 807-819.
[39] A.B.D. Cassie, S. Baxter, Wettability of porous surfaces, Transactions of the Faraday Society, 40 (1944) 546-551.

[40] R.N. Wenzel, Surface roughness and contact angle, The Journal of Physical Chemistry, 53 (1949) 1466-1467.
[41] P.C.Y. Wong, Y.-N. Kwon, C.S. Criddle, Use of atomic force microscopy and fractal geometry to characterize the roughness of nano-, micro-, and ultrafiltration membranes, Journal of Membrane Science, 340 (2009) 117-132.
[42] H.-J. Butt, B. Cappella, M. Kappl, Force measurements with the atomic force microscope: Technique, interpretation and applications, Surface Science Reports, 59 (2005) 1-152.
[43] K. Cooper, N. Ohler, A. Gupta, S. Beaudoin, Analysis of Contact Interactions between a Rough Deformable Colloid and a Smooth Substrate, Journal of Colloid and Interface Science, 222 (2000) 63-74.
[44] K. Cooper, A. Gupta, S. Beaudoin, Simulation of the Adhesion of Particles to Surfaces, Journal of Colloid and Interface Science, 234 (2001) 284-292.
[45] C.S. Hodges, L. Looi, J.A.S. Cleaver, M. Ghadiri, Use of the JKR Model for Calculating Adhesion between Rough Surfaces, Langmuir, 20 (2004) 9571-9576.
[46] L. Zhao, L. Shen, Y. He, H. Hong, H. Lin, Influence of membrane surface roughness on interfacial interactions with sludge flocs in a submerged membrane bioreactor, Journal of Colloid and Interface Science, 446 (2015) 84-90.
[47] Y.I. Rabinovich, J.J. Adler, A. Ata, R.K. Singh, B.M. Moudgil, Adhesion between Nanoscale Rough Surfaces: II. Measurement and Comparison with Theory, Journal of Colloid and Interface Science, 232 (2000) 17-24.
[48] F. Galiano, A. Figoli, S.A. Deowan, D. Johnson, S.A. Altinkaya, L. Veltri, G. De Luca, R. Mancuso, N. Hilal, B. Gabriele, A step forward to a more efficient wastewater treatment by membrane surface modification via polymerizable bicontinuous microemulsion, Journal of Membrane Science, 482 (2015) 103-114.
[49] F. Galiano, I. Friha, S.A. Deowan, J. Hoinkis, Y. Xiaoyun, D. Johnson, R. Mancuso, N. Hilal, B. Gabriele, S. Sayadi, A. Figoli, Novel low-fouling membranes from lab to pilot application in textile wastewater treatment, Journal of Colloid and Interface Science, 515 (2018) 208-220.
[50] Y.T. Chung, E. Mahmoudi, A.W. Mohammad, A. Benamor, D. Johnson, N. Hilal, Development of polysulfone-nanohybrid membranes using ZnO-GO composite for enhanced antifouling and antibacterial control, Desalination, 402 (2017) 123-132.
[51] A. Wahab Mohammad, N. Hilal, M. Nizam Abu Seman, A study on producing composite nanofiltration membranes with optimized properties, Desalination, 158 (2003) 73-78.
[52] S. Al Malek, M.A. Seman, D. Johnson, N. Hilal, Formation and characterization of polyethersulfone membranes using different concentrations of polyvinylpyrrolidone, Desalination, 288 (2012) 31-39.
[53] K. Rasool, K.A. Mahmoud, D.J. . Johnson, M. Helal, G.R. Berdiyorov, Y. Gogotsi, Efficient Antibacterial Membrane based on Two-Dimensional Ti3C2Tx (MXene) Nanosheets, Scientific Reports, 7 (2017) 1598.
[54] D.L. Shaffer, H. Jaramillo, S.R.-V. Castrillón, X. Lu, M. Elimelech, Post-fabrication modification of forward osmosis membranes with a poly (ethylene glycol) block copolymer for improved organic fouling resistance, Journal of Membrane Science, 490 (2015) 209-219.
[55] J. Jung, J. Ryu, S.Y. Choi, K.Y. Park, W.J. Song, Y. Yu, Y.-s. Jang, J. Park, J. Kweon, Autopsy study of irreversible foulants on polyvinylidene fluoride hollow-fiber membranes in an immersed microfiltration system operated for five years, Separation and Purification Technology, 199 (2018) 1-8.
[56] D. Johnson, D. Oatley-Radcliffe, N. Hilal, Atomic Force Microscopy (AFM), Membrane Characterization, (2017) 115.
[57] D. Johnson, S. Al Malek, B. Al-Rashdi, N. Hilal, Atomic force microscopy of nanofiltration membranes: effect of imaging mode and environment, Journal of Membrane Science, 389 (2012) 486-498.
[58] B. Al-Rashdi, D. Johnson, N. Hilal, Removal of heavy metal ions by nanofiltration, Desalination, 315 (2013) 2-17.

[59] K. Boussu, B. Van der Bruggen, A. Volodin, J. Snauwaert, C. Van Haesendonck, C. Vandecasteele, Roughness and hydrophobicity studies of nanofiltration membranes using different modes of AFM, Journal of Colloid and Interface Science, 286 (2005) 632-638.
[60] K. Boussu, B. Van der Bruggen, A. Volodin, C. Van Haesendonck, J.A. Delcour, P. Van der Meeren, C. Vandecasteele, Characterization of commercial nanofiltration membranes and comparison with self-made polyethersulfone membranes, Desalination, 191 (2006) 245-253.
[61] G. Palasantzas, J. Krim, Effect of the form of the height-height correlation function on diffuse x-ray scattering from a self-affine surface, Physical Review B, 48 (1993) 2873-2877.
[62] L. Ponson, H. Auradou, P. Vié, J.-P. Hulin, Low Self-Affine Exponents of Fractured Glass Ceramics Surfaces, Physical Review Letters, 97 (2006) 125501.
[63] S.K. Sinha, E.B. Sirota, S. Garoff, H.B. Stanley, X-ray and neutron scattering from rough surfaces, Physical Review B, 38 (1988) 2297-2311.
[64] Y. Wyart, G. Georges, C. Deumie, C. Amra, P. Moulin, Membrane characterization by microscopic methods: multiscale structure, Journal of Membrane Science, 315 (2008) 82-92.
[65] B. Mandelbrot, The fractal geometry of nature, W.H. Freeman and co., San Francisco, 1982.
[66] B. Mandelbrot, How Long Is the Coast of Britain? Statistical Self-Similarity and Fractional Dimension, science, 156 (1967) 636-638.
[67] M. Zhang, J. Chen, Y. Ma, L. Shen, Y. He, H. Lin, Fractal reconstruction of rough membrane surface related with membrane fouling in a membrane bioreactor, Bioresource Technology, 216 (2016) 817-823.
[68] B.B. Mandelbrot, D.E. Passoja, A.J. Paullay, Fractal character of fracture surfaces of metals, Nature, 308 (1984) 721.
[69] V.Y. Milman, N.A. Stelmashenko, R. Blumenfeld, Fracture surfaces: A critical review of fractal studies and a novel morphological analysis of scanning tunneling microscopy measurements, Progress in Materials Science, 38 (1994) 425-474.
[70] S.M. Wiederhorn, J.M. López-Cepero, J. Wallace, J.-P. Guin, T. Fett, Roughness of glass surfaces formed by sub-critical crack growth, Journal of Non-Crystalline Solids, 353 (2007) 1582-1591.
[71] B.M. Benoit, Self-Affine Fractals and Fractal Dimension, Physica Scripta, 32 (1985) 257.
[72] B.B. Mandelbrot, Self-affine fractals and fractal dimension, Physica Scripta, 32 (1985) 257.
[73] Z. W., Z. A., Fractal Dimension of Thin-film Surfaces Obtained by Fourier Spectral Analysis, Surface and Interface Analysis, 25 (1997) 488-491.
[74] W. Zahn, A. Zösch, Characterization of thin-film surfaces by fractal geometry, Fresenius' Journal of Analytical Chemistry, 358 (1997) 119-121.
[75] J. Schmittbuhl, J.-P. Vilotte, S. Roux, Reliability of self-affine measurements, Physical Review E, 51 (1995) 131-147.
[76] C. Douketis, Z. Wang, T.L. Haslett, M. Moskovits, Fractal character of cold-deposited silver films determined by low-temperature scanning tunneling microscopy, Physical Review B, 51 (1995) 11022-11031.
[77] C. Gibson, G.S. Watson, S. Myhra, Scanning force microscopy—calibrative procedures for 'best practice', Scanning, 19 (1997) 564-581.
[78] T.D. Jacobs, T. Junge, L. Pastewka, Quantitative characterization of surface topography using spectral analysis, Surface Topography: Metrology and Properties, 5 (2017) 013001.
[79] L.D. Nghiem, D. Vogel, S. Khan, Characterising humic acid fouling of nanofiltration membranes using bisphenol A as a molecular indicator, Water research, 42 (2008) 4049-4058.
[80] N. Hilal, H. Al-Zoubi, N. Darwish, A.W. Mohammad, Characterisation of nanofiltration membranes using atomic force microscopy, Desalination, 177 (2005) 187-199.
[81] A. Gautam, T.J. Menkhaus, Performance evaluation and fouling analysis for reverse osmosis and nanofiltration membranes during processing of lignocellulosic biomass hydrolysate, Journal of Membrane Science, 451 (2014) 252-265.

[82] A.L. Carvalho, F. Maugeri, V. Silva, A. Hernández, L. Palacio, P. Pradanos, AFM analysis of the surface of nanoporous membranes: application to the nanofiltration of potassium clavulanate, Journal of Materials Science, 46 (2011) 3356-3369.
[83] V. Freger, J. Gilron, S. Belfer, TFC polyamide membranes modified by grafting of hydrophilic polymers: an FT-IR/AFM/TEM study, Journal of Membrane Science, 209 (2002) 283-292.
[84] D.J. Johnson, D.L. Oatley-Radcliffe, N. Hilal, State of the art review on membrane surface characterisation: Visualisation, verification and quantification of membrane properties, Desalination, 434 (2018) 12-36.
[85] F. Lapique, P. Meakin, J. Feder, T. Jøssang, Self-affine fractal scaling in fracture surfaces generated in ethylene and propylene polymers and copolymers, Journal of applied polymer science, 86 (2002) 973-983.
[86] J. Gagnepain, C. Roques-Carmes, Fractal approach to two-dimensional and three-dimensional surface roughness, Wear, 109 (1986) 119-126.
[87] Bruker, Nanoscope 1.8 Manual.
[88] P. Klapetek, I. Ohlídal, J. Bílek, Influence of the atomic force microscope tip on the multifractal analysis of rough surfaces, Ultramicroscopy, 102 (2004) 51-59.
[89] W. Zahn, A. Zösch, The dependence of fractal dimension on measuring conditions of scanning probe microscopy, Fresenius' Journal of Analytical Chemistry, 365 (1999) 168-172.
[90] J. Krim, J.O. Indekeu, Roughness exponents: A paradox resolved, Physical Review E, 48 (1993) 1576-1578.

**Figure Captions**

Figure 1: Representative AFM height images of Dow NF270 nanofiltration membrane surface. All images taken from a single locus, with the scan length increased stepwise at values of A: 1 µm; B: 2 µm; C: 5 µm; D: 10 µm; E: 20 µm; F: 40 µm; G: 80 µm.

Figure 2: Representative AFM height images of Dow BW30 membrane surface. All images taken from a single locus, with the scan length increased stepwise at values of A: 1 µm; B: 2 µm; C: 5 µm; D: 10 µm; E: 20 µm; F: 40 µm; G: 80 µm.

Figure 3: Representative AFM height images of Dow NF90 membrane surface. All images taken from a single locus, with the scan length increased stepwise at values of A: 1 µm; B: 2 µm; C: 5 µm; D: 10 µm; E: 20 µm; F: 40 µm; G: 80 µm.

Figure 4: Representative AFM height images of Koch TFC-SR3 membrane surface. All images taken from a single locus, with the scan length increased stepwise at values of A: 1 µm; B: 2 µm; C: 5 µm; D: 10 µm; E: 20 µm; F: 40 µm; G: 80 µm.

Figure 5: Plot of mean RMS roughness, $R_q$, against the scan length for polymer membranes: A) Dow NF270; B) Dow BW30; C) Dow NF90; D) Koch TFC-SR3. Error bars represent standard deviation.

Figure 6 Plot of natural logs of $R_q$ versus scan size for polymer membranes: A) Dow NF270; B) Dow BW30; C) Dow NF90; D) Koch TFC-SR3. Error bars represent standard deviation.

Figure 7: Example linear fits to the a) power spectra and b) integrated power spectra (eq. 6) of AFM images.

Figure 8: Comparison of roughness exponent calculated by each method for each membrane plotted versus scan size. Error bars show standard deviation. Dashed lines represent H values calculated from log-log plots.

Figure 9: Values of Rq for different scan sizes calculated using $R_q$ values and $H_a$ (left side figures) and $H_b$ (right side figures) obtained at discrete scan sizes of 1 to 10 µm for membrane samples: a) NF270; b) BW30; c) NF90; d) TFC-SR3.

Figure 10: Values of a) $H_a$ and b) $H_b$ calculated for NF270 membrane versus the cumulative number of measurements for each scan size.

**Figures**

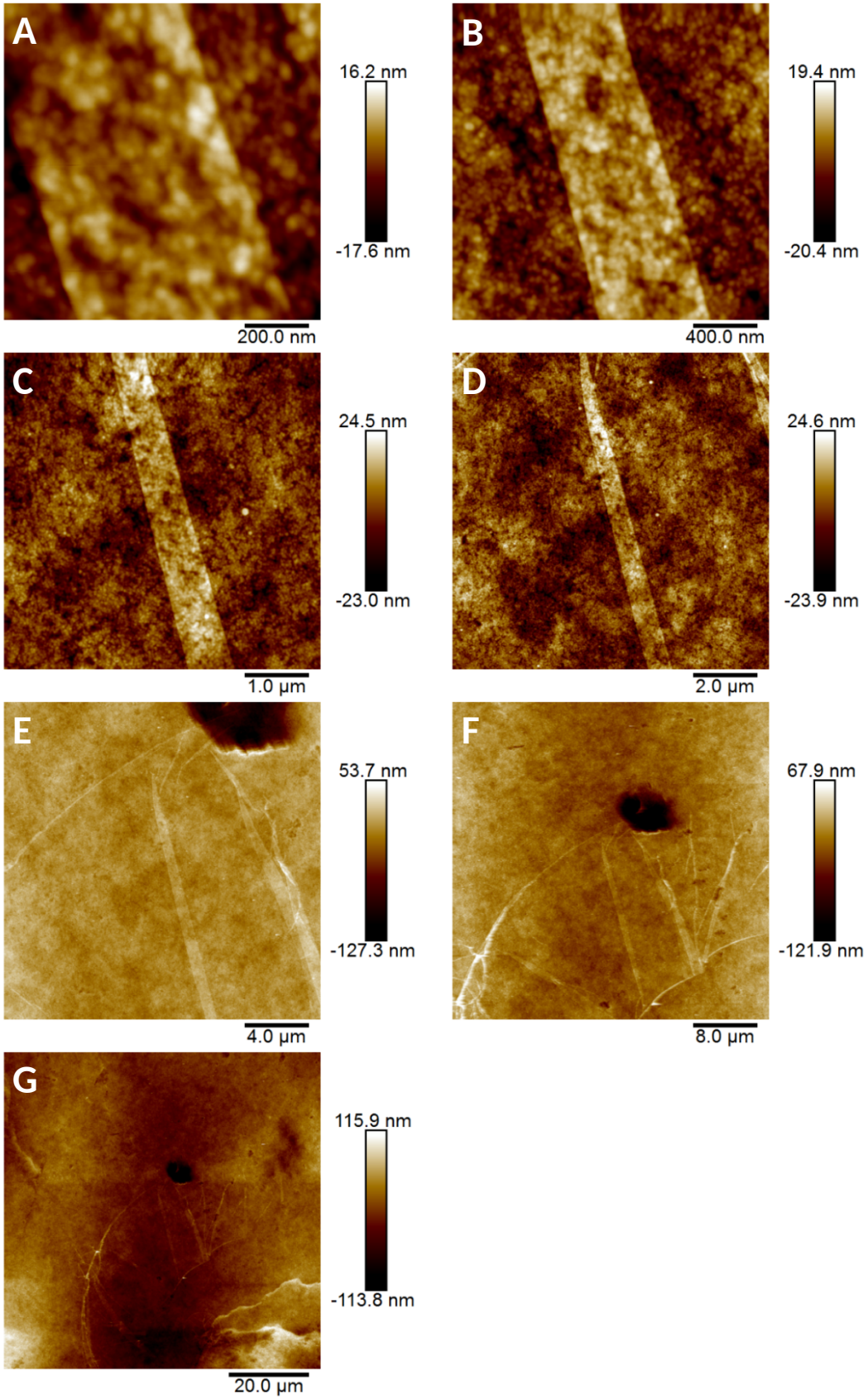


Figure 1

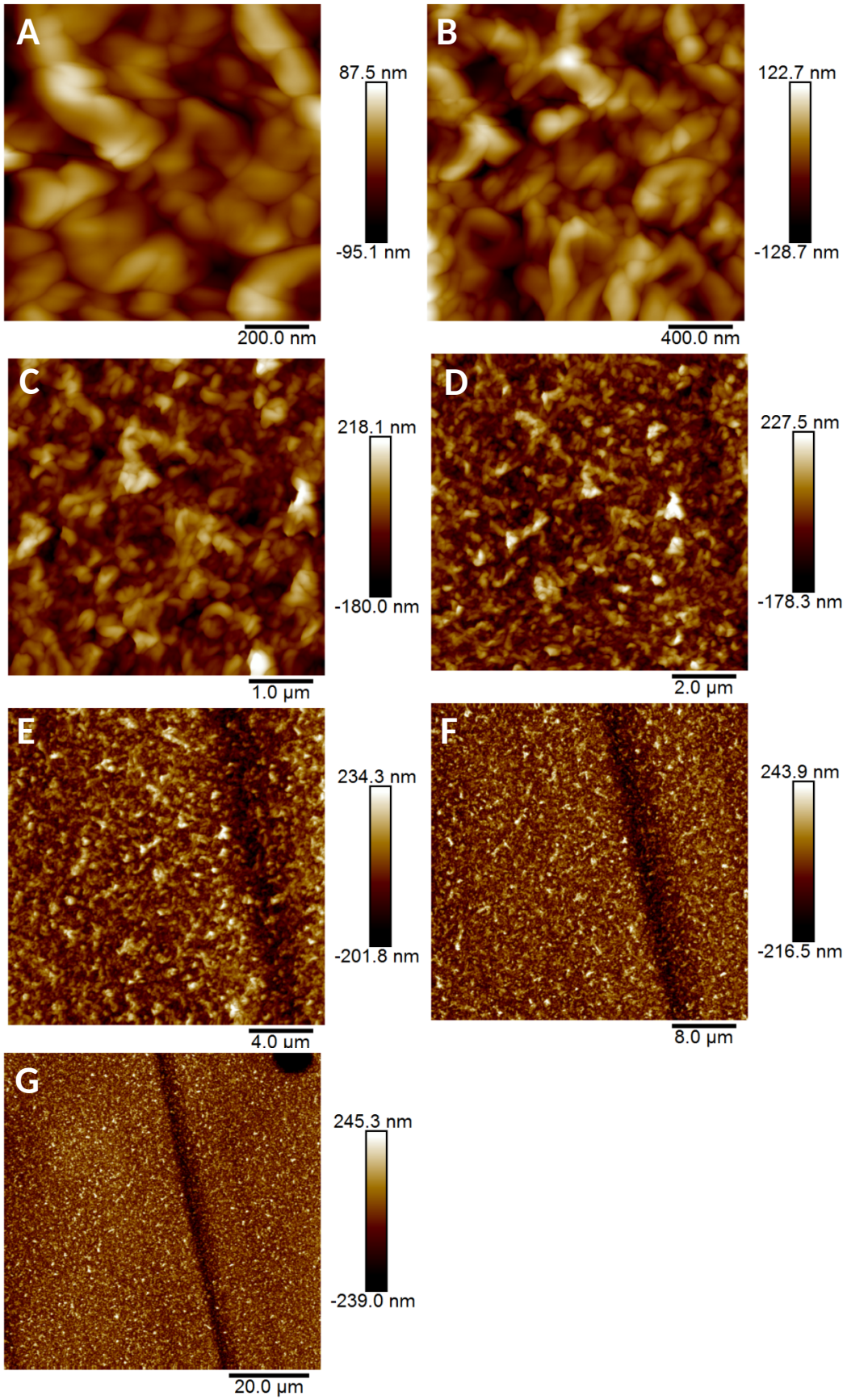
A
87.5 nm
-95.1 nm
200.0 nm
B
122.7 nm
-128.7 nm
400.0 nm
C
218.1 nm
-180.0 nm
1.0 µm
D
227.5 nm
-178.3 nm
2.0 µm
E
234.3 nm
-201.8 nm
4.0 µm
F
243.9 nm
-216.5 nm
8.0 µm
G
245.3 nm
-239.0 nm
20.0 µm

Figure 2

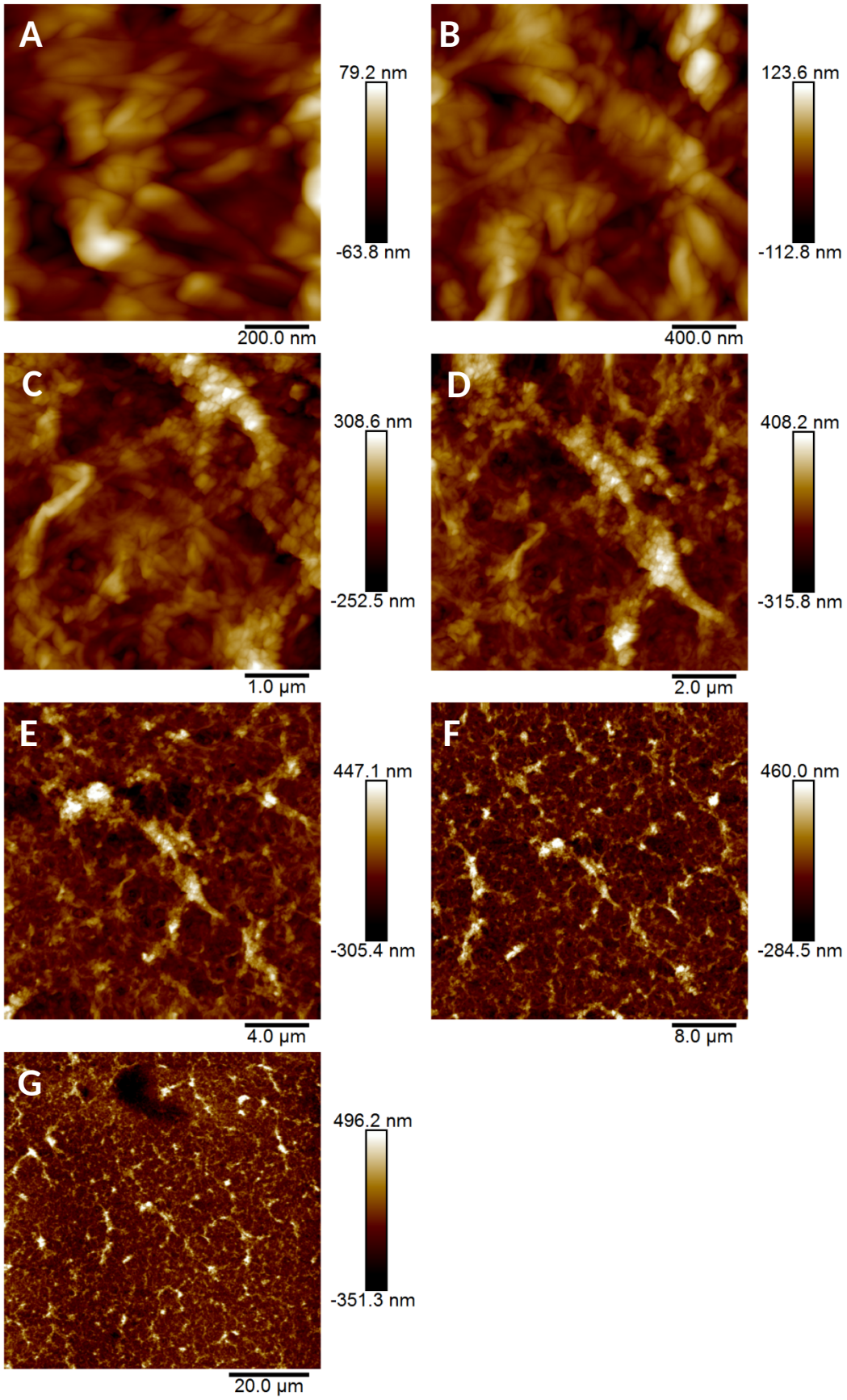
A
79.2 nm
-63.8 nm
200.0 nm
B
123.6 nm
-112.8 nm
400.0 nm
C
308.6 nm
-252.5 nm
1.0 µm
D
408.2 nm
-315.8 nm
2.0 µm
E
447.1 nm
-305.4 nm
4.0 µm
F
460.0 nm
-284.5 nm
8.0 µm
G
496.2 nm
-351.3 nm
20.0 µm

Figure 3

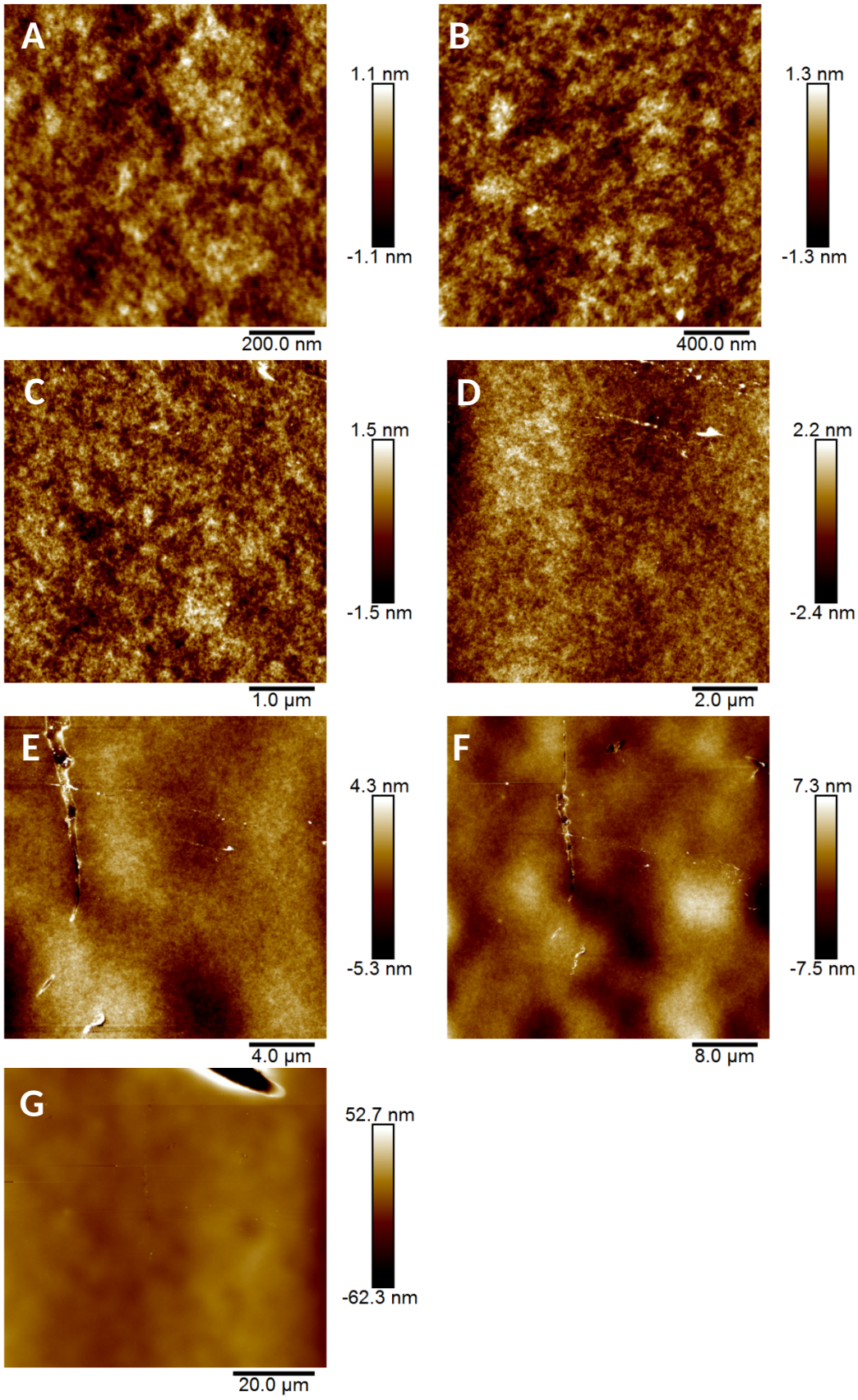
A
1.1 nm
-1.1 nm
200.0 nm
B
1.3 nm
-1.3 nm
400.0 nm
C
1.5 nm
-1.5 nm
1.0 µm
D
2.2 nm
-2.4 nm
2.0 µm
E
4.3 nm
-5.3 nm
4.0 µm
F
7.3 nm
-7.5 nm
8.0 µm
G
52.7 nm
-62.3 nm
20.0 µm

Figure 4

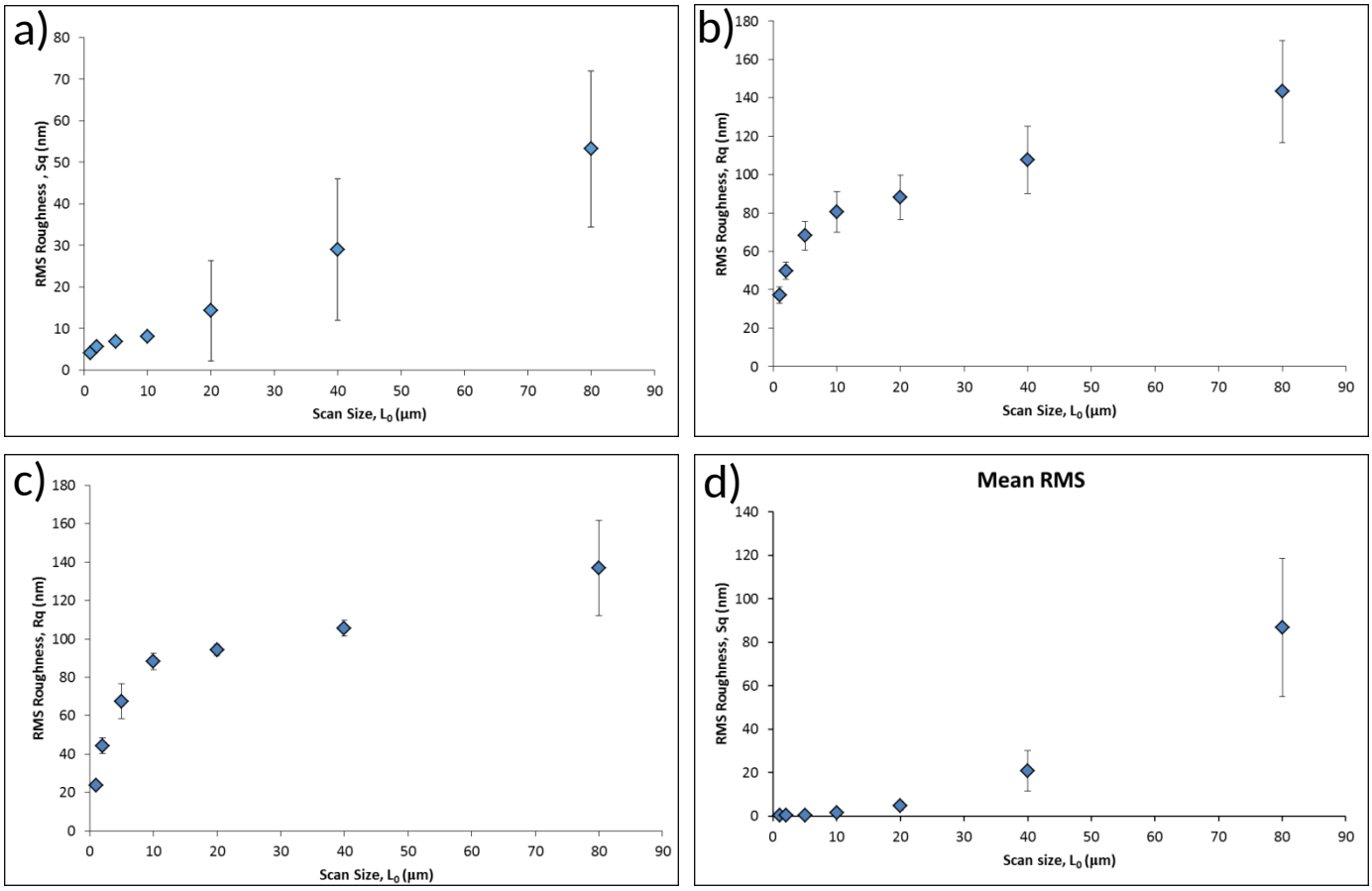
a)
RMS Roughness , Sq (nm)
Scan Size, L0 (µm)
b)
RMS Roughness, Rq (nm)
Scan Size, L0 (µm)
c)
RMS Roughness, Rq (nm)
Scan Size, L0 (µm)
d)
Mean RMS
RMS Roughness, Sq (nm)
Scan size, L0 (µm)

Figure 5

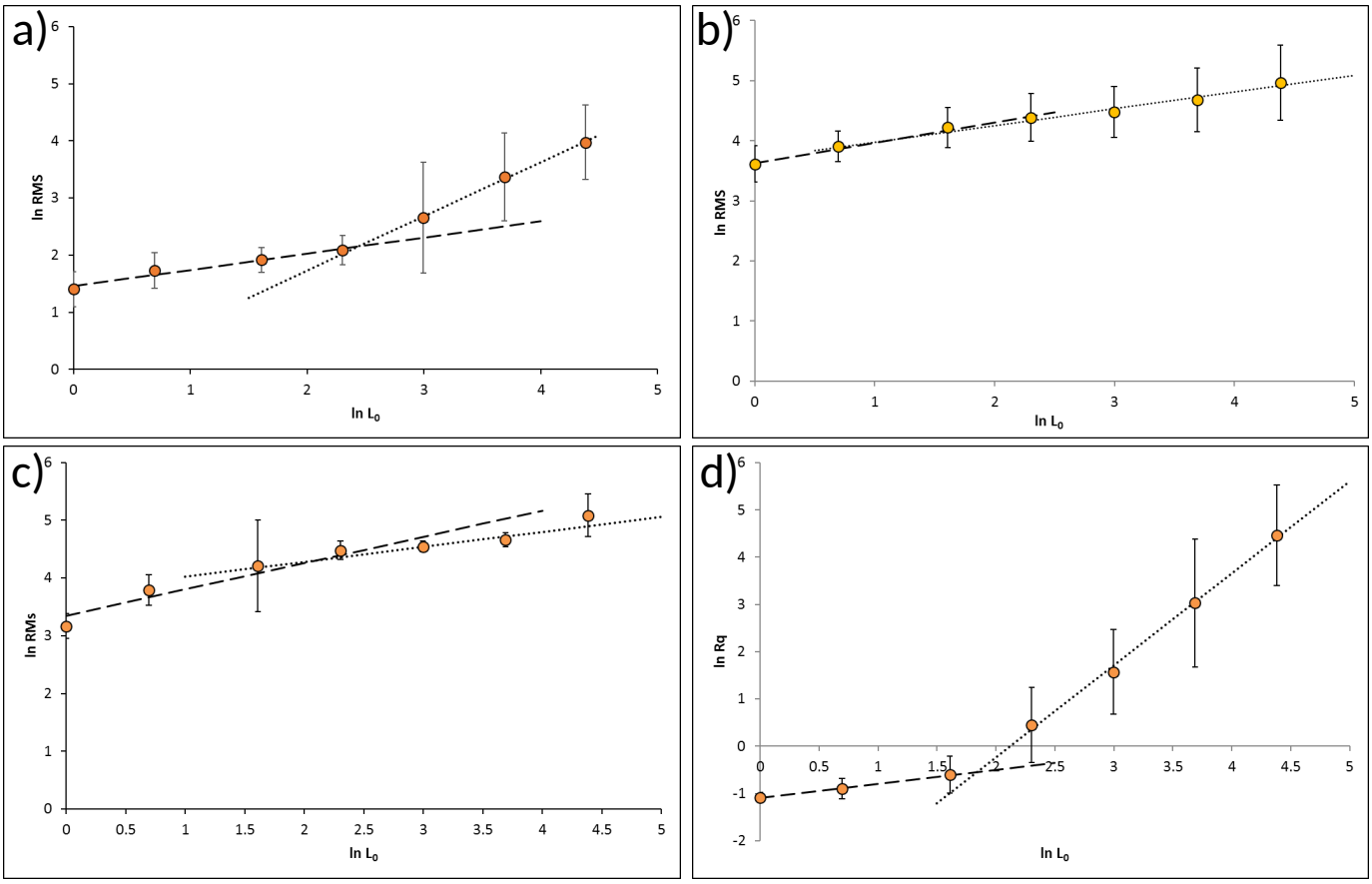


Figure 6

a)

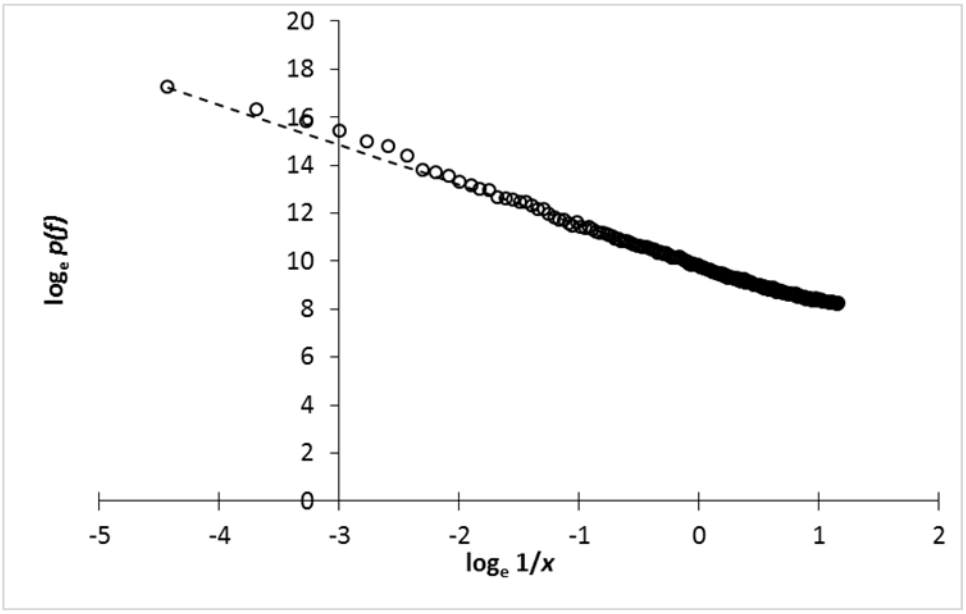
20
18
16
14
12
10
8
6
4
2
0
-5
-4
-3
-2
-1
0
1
2
log$_e$ p(f)
log$_e$ 1/x

b)

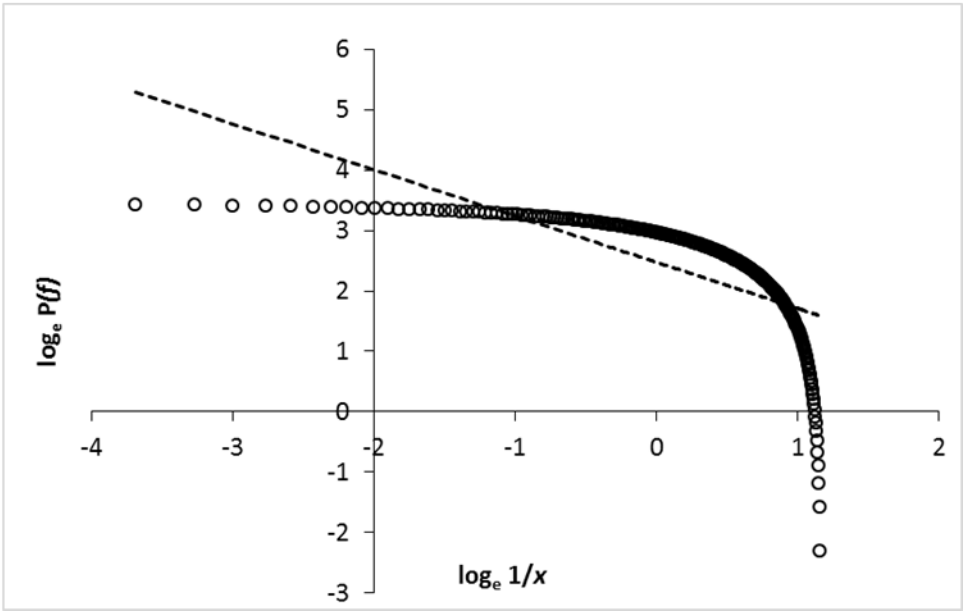
6
5
4
3
2
1
0
-1
-2
-3
-4
-3
-2
-1
0
1
2
log$_e$ P(f)
log$_e$ 1/x

Figure 7

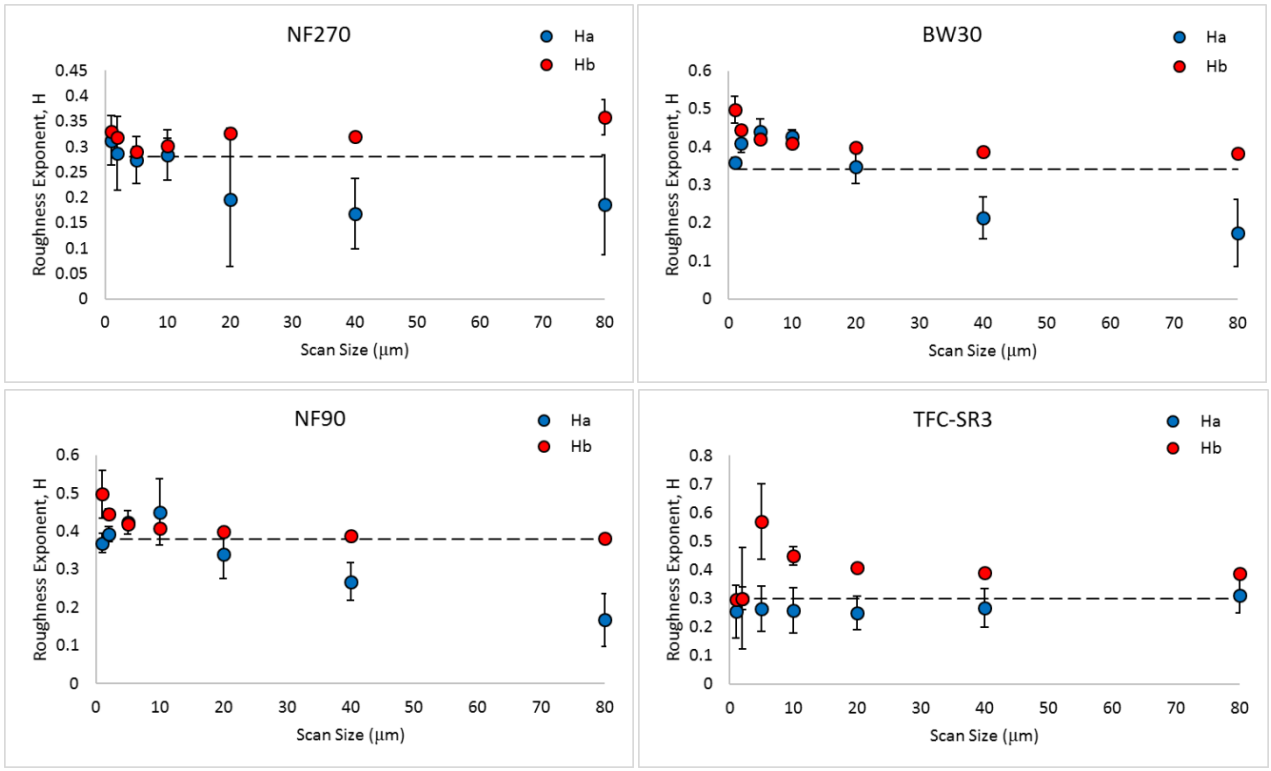
NF270
Ha
Hb
Roughness Exponent, H
Scan Size (μm)
BW30
NF90
TFC-SR3

Figure 8

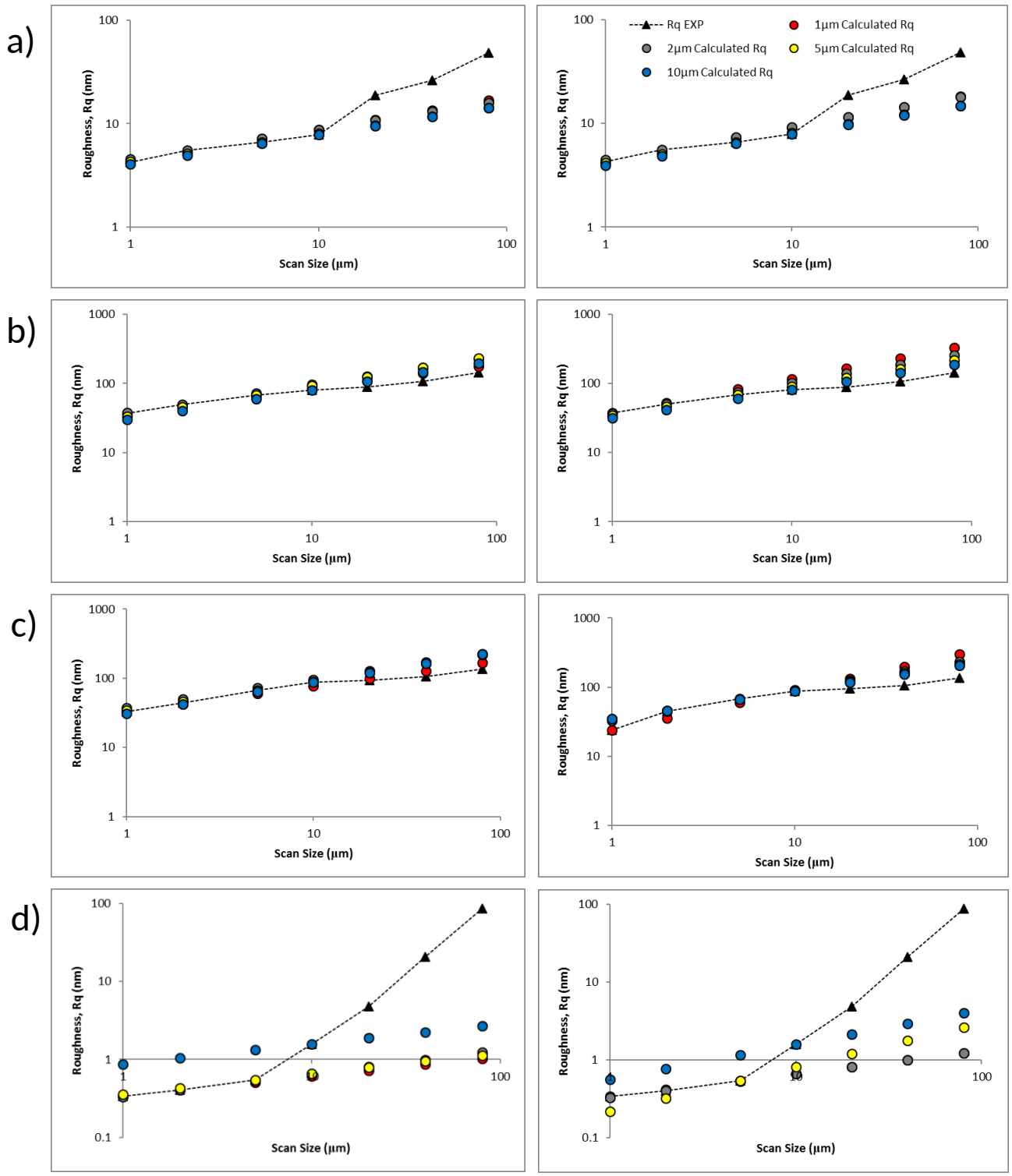
a)
b)
c)
d)
Roughness, Rq (nm)
Scan Size (µm)
Rq EXP
1µm Calculated Rq
2µm Calculated Rq
5µm Calculated Rq
10µm Calculated Rq

Figure 9

a)

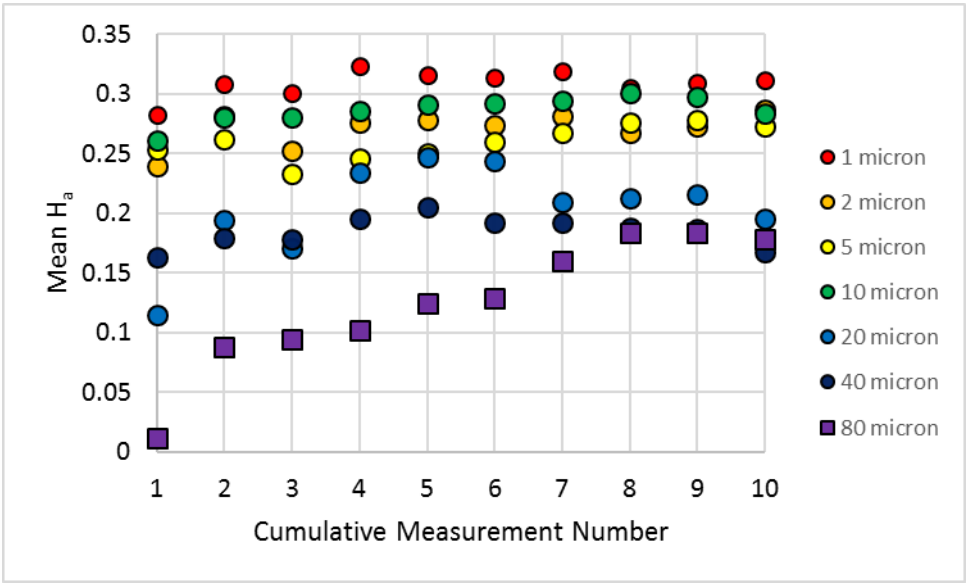
0.35
0.3
0.25
0.2
0.15
0.1
0.05
0
Mean $H_a$
1
2
3
4
5
6
7
8
9
10
Cumulative Measurement Number
1 micron
2 micron
5 micron
10 micron
20 micron
40 micron
80 micron

b)

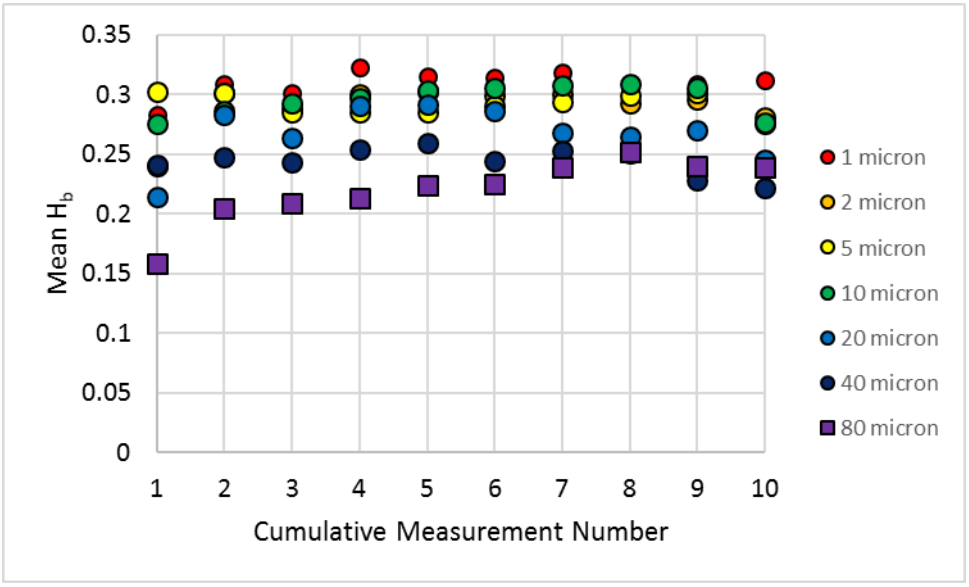
0.35
0.3
0.25
0.2
0.15
0.1
0.05
0
Mean $H_b$
1
2
3
4
5
6
7
8
9
10
Cumulative Measurement Number
1 micron
2 micron
5 micron
10 micron
20 micron
40 micron
80 micron

Figure 10

**Table Captions**

Table 1: Comparison of literature values for *Rq* with those from this work.

Table 2: Values of slope calculated using linear regression from log-log plots of Rq versus scan size for slopes in lower and upper bounds of the scan size range with calculated crossover length. Values in brackets are confidence interval calculated for 98% confidence level.

| Membrane | Rq (nm) | Scan Size (μm) | Value from this work (nm) | Ref. |
|---|---|---|---|---|
| NF270 | 3.0 | 1 | 4.8 | [57] |
| | 2.47-4.94 | 1 | 4.8 | [58] |
| | 3.36 | 2 | 6.25 | [80] |
| | 8.55 | 2 | 6.25 | [79] |
| | 23.67 | 10 | 8.46 | [36] |
| BW30 | 53.9 | 10 | 80.5 | [36] |
| | 76.8 | 20 | 88.5 | [81] |
| NF90 | 22.8 | 2 | 44.35 | [80] |
| | 76.8 | 2 | 44.35 | [79] |
| TFC-SR3 | 8.0 | 20 | 4.82 | [81] |

Table 1

| | Lower | Upper | Crossover length (μm) |
|---|---|---|---|
| NF270 | 0.28 (± 0.18) | 0.92 (± 0.12) | 11.48 |
| BW30 | 0.33 (± 0.12) | 0.21 (± 0.20) | 3.34 |
| NF90 | 0.56 (± 0.35) | 0.28 (± 0.39) | 8.25 |
| TFC-SR3 | 0.30 (± 0.30) | 1.95 (± 0.30) | 6.29 |

Table 2

**Supplementary Table Captions**

Table S1: Fractal dimension values calculated from equation 5 ($D_{Ha}$) and equation 7 ($D_{Hb}$). Corresponding standard deviation values are shown in brackets.

Table S2: Tabulated values ($H_a$, a, scan size, $R_q$) used to recalculated $R_q$ values at 1,2,5,10 μm from power spectra derived $H_a$.

Table S3: Tabulated values ($H_b$, a, scan size, $R_q$) used to recalculated $R_q$ values at 1, 2, 5, 10 μm from integrated power spectra derived $H_b$.

Table S4: Absolute percentage errors for calculated Rq values calculated from $H_a$ values obtained from image power spectra versus experimentally derived values; relative standard error of AFM Rq measurements and cumulative errors combining the two.

Table S5: Absolute percentage errors for calculated Rq values calculated from $H_b$ values obtained from image power spectra versus experimentally derived values; relative standard error of AFM Rq measurements and cumulative errors combining the two.

Table S1:

| | Scan Size (μm) | Mean $D_{Ha}$ (s.d.) | Mean $D_{Hb}$ (s.d.) |
|---|---|---|---|
| **Dow NF270** | **1** | 1.688 (0.049) | 1.669 (0.002) |
| | **2** | 1.713 (0.073) | 1.683 (0.008) |
| | **5** | 1.727 (0.0467) | 1.709 (0.009) |
| | **10** | 1.717 (0.050) | 1.698 (0.015) |
| | **20** | 1.804 (0.132) | 1.673 (0.010) |
| | **40** | 1.833 (0.070) | 1.780 (0.007) |
| | **80** | 1.814 (0.099) | 1.643 (0.035) |
| **Dow BW30** | **1** | 1.641 (0.013) | 1.503 (0.035) |
| | **2** | 1.590 (0.024) | 1.554 (0.007) |
| | **5** | 1.558 (0.033) | 1.583 (0.010) |
| | **10** | 1.572 (0.017) | 1.591 (0.006) |
| | **20** | 1.652 (0.045) | 1.601 (0.007) |
| | **40** | 1.786 (0.054) | 1.612 (0.003) |
| | **80** | 1.826 (0.088) | 1.618 (0.001) |
| **Dow NF90** | **1** | 1.632 (0.025) | 1.423 (0.063) |
| | **2** | 1.608 (0.021) | 1.552 (0.012) |
| | **5** | 1.577 (0.031 | 1.584 (0.007) |
| | **10** | 1.550 (0.087) | 1.575 (0.004) |
| | **20** | 1.661 (0.064) | 1.606 (0.005) |
| | **40** | 1.733 (0.050) | 1.612 (0.004) |
| | **80** | 1.833 (0.070) | 1.621 (0.004) |
| **Koch TFC** | **1** | 1.763 (0.092) | 1.706 (0.009) |
| | **2** | 1.646 (0.177) | 1.706 (0.009) |
| | **5** | 1.736 (0.079) | 1.432 (0.133) |
| | **10** | 1.743 (0.079) | 1.551 (0.032) |
| | **20** | 1.752 (0.059) | 1.593 (0.008) |
| | **40** | 1.734 (0.069) | 1.610 (0.007) |
| | **80** | 1.689 (0.063) | 1.614 (0.004) |

Table S2:

| Dow NF270 | | | | | | | | | |
|---|---|---|---|---|---|---|---|---|---|
| $L_0$ (µm) | $H_a$ | $R_q$ (nm) | ln $L_0$ | ln $R_q$ | A | $R_q$ (1 µm) | $R_q$ (2 µm) | $R_q$ (5 µm) | $R_q$ (10 µm) |
| 1 | 0.312 | 4.2737 | 0 | 1.45248 | 4.2737 | 4.2737 | 4.548806 | 4.283258 | 4.098592 |
| 2 | 0.287 | 5.55 | 0.693147 | 1.713798 | 4.548806 | 5.305489 | 5.55 | 5.175537 | 4.988578 |
| 5 | 0.273 | 6.6465 | 1.609438 | 1.89409 | 4.283258 | 7.061268 | 7.219411 | 6.6465 | 6.468338 |
| 10 | 0.2835 | 7.8729 | 2.302585 | 2.063426 | 4.098592 | 8.766052 | 8.808407 | 8.031085 | 7.8729 |
| 20 | 0.19562 | 18.7859 | 2.995732 | 2.933107 | 10.45501 | 10.88242 | 10.74714 | 9.704103 | 9.582454 |
| 40 | 0.167333 | 26.41378 | 3.688879 | 3.273886 | 14.24795 | 13.50973 | 13.11259 | 11.72564 | 11.66323 |
| 80 | 0.185778 | 48.25167 | 4.382027 | 3.87643 | 21.37768 | 16.77135 | 15.99868 | 14.1683 | 14.19583 |
| | | | | | | | | | |
| **Dow BW30** | | | | | | | | | |
| $L_0$ (µm) | $H_a$ | $R_q$ (nm) | ln $L_0$ | ln $R_q$ | A | $R_q$ (1 µm) | $R_q$ (2 µm) | $R_q$ (5 µm) | $R_q$ (10 µm) |
| 1 | 0.358553 | 37.1635 | 0 | 3.615327 | 37.1635 | 37.1635 | 37.50839 | 33.54747 | 30.08506 |
| 2 | 0.410088 | 49.8399 | 0.693147 | 3.908816 | 37.50839 | 47.64878 | 49.8399 | 45.5119 | 40.46409 |
| 5 | 0.44004 | 68.1137 | 1.609438 | 4.221178 | 33.54747 | 66.18116 | 72.57175 | 68.1137 | 59.87243 |
| 10 | 0.427595 | 80.5278 | 2.302585 | 4.388602 | 30.08506 | 84.85347 | 96.43093 | 92.4059 | 80.5278 |
| 20 | 0.347849 | 88.0819 | 2.995732 | 4.478267 | 31.06882 | 108.794 | 128.1342 | 125.3617 | 108.3091 |
| 40 | 0.213508 | 107.6206 | 3.688879 | 4.678612 | 48.96008 | 139.489 | 170.2605 | 170.071 | 145.6745 |
| 80 | 0.173978 | 143.1971 | 4.382027 | 4.964222 | 66.80953 | 178.8444 | 226.2365 | 230.7254 | 195.9307 |
| | | | | | | | | | |
| **Dow NF90** | | | | | | | | | |
| $L_0$ (µm) | $H_a$ | $R_q$ (nm) | ln $L_0$ | ln $R_q$ | A | $R_q$ (1 µm) | $R_q$ (2 µm) | $R_q$ (5 µm) | $R_q$ (10 µm) |
| 1 | 0.368494 | 33.11545 | 0 | 3.5 | 33.11545 | 33.11545 | 33.79288 | 34.17071 | 31.30036 |
| 2 | 0.392462 | 44.3576 | 0.693147 | 3.792284 | 33.79288 | 42.7522 | 44.3576 | 45.82682 | 42.75953 |
| 5 | 0.423432 | 67.5492 | 1.609438 | 4.212856 | 34.17071 | 59.92347 | 63.55422 | 67.5492 | 64.58514 |
| 10 | 0.450067 | 88.23 | 2.302585 | 4.479947 | 31.30036 | 77.36147 | 83.42327 | 90.59119 | 88.23 |
| 20 | 0.339202 | 94.2438 | 2.995732 | 4.545885 | 34.11466 | 99.874 | 109.504 | 121.4931 | 120.5313 |
| 40 | 0.267405 | 105.6294 | 3.688879 | 4.659937 | 39.39001 | 128.9378 | 143.7384 | 162.9361 | 164.6583 |
| 80 | 0.166781 | 137 | 4.382027 | 4.919981 | 65.96618 | 166.4592 | 188.6756 | 218.5159 | 224.9403 |
| | | | | | | | | | |
| **Koch TFC** | | | | | | | | | |
| $L_0$ (µm) | $H_a$ | $R_q$ (nm) | ln $L_0$ | ln $R_q$ | A | $R_q$ (1 µm) | $R_q$ (2 µm) | $R_q$ (5 µm) | $R_q$ (10 µm) |
| 1 | 0.253929 | 0.33775 | 0 | -1.08545 | 0.33775 | 0.33775 | 0.329884 | 0.356729 | 0.871355 |
| 2 | 0.299877 | 0.4061 | 0.693147 | -0.90116 | 0.329884 | 0.40275 | 0.4061 | 0.428263 | 1.041303 |
| 5 | 0.263669 | 0.5453 | 1.609438 | -0.60642 | 0.356729 | 0.508258 | 0.534523 | 0.5453 | 1.317865 |
| 10 | 0.257058 | 1.5749 | 2.302585 | 0.454192 | 0.871355 | 0.606072 | 0.658018 | 0.654648 | 1.5749 |
| 20 | 0.248234 | 4.81671 | 2.995732 | 1.572091 | 2.289763 | 0.722711 | 0.810047 | 0.785923 | 1.882067 |
| 40 | 0.265932 | 20.7749 | 3.688879 | 3.033746 | 7.789327 | 0.861797 | 0.997199 | 0.943523 | 2.249144 |
| 80 | 0.310924 | 86.8751 | 4.382027 | 4.464471 | 22.24226 | 1.02765 | 1.227592 | 1.132725 | 2.687816 |

Table S3:

| Dow NF270 | | | | | | | | | |
|---|---|---|---|---|---|---|---|---|---|
| $L_0$ (µm) | $H_a$ | $R_q$ (nm) | ln $L_0$ | ln $R_q$ | A | $R_q$ (1 µm) | $R_q$ (2 µm) | $R_q$ (5 µm) | $R_q$ (10 µm) |
| 1 | 0.3306 | 4.2737 | 0 | 1.45248 | 4.2737 | 4.2737 | 4.453649 | 4.162292 | 3.924052 |
| 2 | 0.3175 | 5.55 | 0.693147 | 1.713798 | 4.453649 | 5.374333 | 5.55 | 5.091808 | 4.839118 |
| 5 | 0.2908 | 6.6465 | 1.609438 | 1.89409 | 4.162292 | 7.275846 | 7.424017 | 6.6465 | 6.384153 |
| 10 | 0.3024 | 7.8729 | 2.302585 | 2.063426 | 3.924052 | 9.149641 | 9.251581 | 8.130786 | 7.8729 |
| 20 | 0.3271 | 18.7859 | 2.995732 | 2.933107 | 7.051233 | 11.506 | 11.52904 | 9.94654 | 9.708815 |
| 40 | 0.320333 | 26.41378 | 3.688879 | 3.273886 | 8.102841 | 14.46922 | 14.36713 | 12.16779 | 11.97285 |
| 80 | 0.357222 | 48.25167 | 4.382027 | 3.87643 | 10.08524 | 18.19557 | 17.90387 | 14.88508 | 14.76485 |
| | | | | | | | | | |
| **Dow BW30** | | | | | | | | | |
| $L_0$ (µm) | $H_a$ | $R_q$ (nm) | ln $L_0$ | ln $R_q$ | A | $R_q$ (1 µm) | $R_q$ (2 µm) | $R_q$ (5 µm) | $R_q$ (10 µm) |
| 1 | 0.497389 | 37.1635 | 0 | 3.615327 | 37.1635 | 37.1635 | 36.60188 | 34.67147 | 31.43244 |
| 2 | 0.445384 | 49.8399 | 0.693147 | 3.908816 | 36.60188 | 52.46211 | 49.8399 | 46.37388 | 41.7224 |
| 5 | 0.419563 | 68.1137 | 1.609438 | 4.221178 | 34.67147 | 82.75169 | 74.95715 | 68.1137 | 60.6673 |
| 10 | 0.408568 | 80.5278 | 2.302585 | 4.388602 | 31.43244 | 116.817 | 102.0674 | 91.10362 | 80.5278 |
| 20 | 0.398447 | 88.0819 | 2.995732 | 4.478267 | 26.69904 | 164.9055 | 138.9827 | 121.8532 | 106.89 |
| 40 | 0.387396 | 107.6206 | 3.688879 | 4.678612 | 25.77891 | 232.79 | 189.2494 | 162.9814 | 141.8823 |
| 80 | 0.382067 | 143.1971 | 4.382027 | 4.964222 | 26.84269 | 328.6195 | 257.6963 | 217.9913 | 188.3299 |
| | | | | | | | | | |
| **Dow NF90** | | | | | | | | | |
| $L_0$ (µm) | $H_a$ | $R_q$ (nm) | ln $L_0$ | ln $R_q$ | A | $R_q$ (1 µm) | $R_q$ (2 µm) | $R_q$ (5 µm) | $R_q$ (10 µm) |
| 1 | 0.576669 | 23.7535 | 0 | 3.16773 | 23.7535 | 23.7535 | 32.51888 | 34.60044 | 34.71369 |
| 2 | 0.447904 | 44.3576 | 0.693147 | 3.792284 | 32.51888 | 35.42602 | 44.3576 | 46.15405 | 45.96769 |
| 5 | 0.415667 | 67.5492 | 1.609438 | 4.212856 | 34.60044 | 60.08997 | 66.86622 | 67.5492 | 66.62916 |
| 10 | 0.405116 | 88.23 | 2.302585 | 4.479947 | 34.71369 | 89.6183 | 91.20932 | 90.10489 | 88.23 |
| 20 | 0.39406 | 94.2438 | 2.995732 | 4.545885 | 28.94466 | 133.6569 | 124.4147 | 120.1923 | 116.8337 |
| 40 | 0.388342 | 105.6294 | 3.688879 | 4.659937 | 25.21376 | 199.3362 | 169.7087 | 160.3263 | 154.7106 |
| 80 | 0.379096 | 137 | 4.382027 | 4.919981 | 26.01757 | 297.2903 | 231.4923 | 213.8616 | 204.867 |
| | | | | | | | | | |
| **Koch TFC** | | | | | | | | | |
| $L_0$ (µm) | $H_a$ | $R_q$ (nm) | ln $L_0$ | ln $R_q$ | A | $R_q$ (1 µm) | $R_q$ (2 µm) | $R_q$ (5 µm) | $R_q$ (10 µm) |
| 1 | 0.295921 | 0.33775 | 0 | -1.08545 | 0.33775 | 0.33775 | 0.329884 | 0.218618 | 0.560526 |
| 2 | 0.299877 | 0.4061 | 0.693147 | -0.90116 | 0.329884 | 0.414645 | 0.4061 | 0.324073 | 0.764989 |
| 5 | 0.567907 | 0.5453 | 1.609438 | -0.60642 | 0.218618 | 0.543795 | 0.534523 | 0.5453 | 1.153968 |
| 10 | 0.448657 | 1.5749 | 2.302585 | 0.454192 | 0.560526 | 0.6676 | 0.658018 | 0.808337 | 1.5749 |
| 20 | 0.406939 | 4.81671 | 2.995732 | 1.572091 | 1.423345 | 0.819592 | 0.810047 | 1.198255 | 2.149375 |
| 40 | 0.390441 | 20.7749 | 3.688879 | 3.033746 | 4.920719 | 1.006187 | 0.997199 | 1.776259 | 2.933401 |
| 80 | 0.386119 | 86.8751 | 4.382027 | 4.464471 | 15.99837 | 1.235265 | 1.227592 | 2.633074 | 4.003415 |

Table S4:

| | | Percentage Error (%) | | | | Relative SE Rq (%) | Cumulative Error (%) | | | |
|---|---|---|---|---|---|---|---|---|---|---|
| | $L_0$ (µm) | 1 | 2 | 5 | 10 | | 1 | 2 | 5 | 10 |
| NF270 | 1 | 0 | 6.4 | 0.2 | 4.1 | 13.9 | 13.9 | 15.3 | 13.9 | 14.5 |
| | 2 | 4.4 | 0 | 6.7 | 10.1 | 12.8 | 13.5 | 12.8 | 14.5 | 16.3 |
| | 5 | 6.2 | 8.6 | 0 | 2.7 | 8 | 10.2 | 11.8 | 8 | 8.4 |
| | 10 | 11.3 | 11.9 | 2 | 0 | 9.2 | 14.6 | 15 | 9.4 | 9.2 |
| | 20 | 42.1 | 42.8 | 48.3 | 49 | 64.2 | 76.8 | 77.2 | 80.4 | 80.8 |
| | 40 | 48.9 | 50.4 | 55.6 | 55.8 | 64.5 | 80.9 | 81.8 | 85.2 | 85.3 |
| | 80 | 65.2 | 66.8 | 70.6 | 70.6 | 38.9 | 76 | 77.3 | 80.7 | 80.6 |
| BW30 | 1 | 0 | 0.9 | 9.7 | 19 | 11.2 | 11.2 | 11.2 | 14.8 | 22.1 |
| | 2 | 4.4 | 0 | 8.7 | 18.8 | 9.1 | 10.1 | 9.1 | 12.6 | 20.9 |
| | 5 | 2.8 | 6.5 | 0 | 12.1 | 10.7 | 11.1 | 12.6 | 10.7 | 16.2 |
| | 10 | 5.4 | 19.7 | 14.8 | 0 | 13.1 | 14.1 | 23.7 | 19.7 | 13.1 |
| | 20 | 23.5 | 45.5 | 42.3 | 23 | 13.1 | 26.9 | 47.3 | 44.3 | 26.4 |
| | 40 | 29.6 | 58.2 | 58 | 35.4 | 16.2 | 33.8 | 60.4 | 60.3 | 38.9 |
| | 80 | 24.9 | 58 | 61.1 | 36.8 | 18.6 | 31.1 | 60.9 | 63.9 | 41.3 |
| NF90 | 1 | 0 | 2 | 3.2 | 5.5 | 5.5 | 5.5 | 5.9 | 6.4 | 7.8 |
| | 2 | 3.6 | 0 | 3.3 | 3.6 | 9.5 | 10.1 | 9.5 | 10 | 10.1 |
| | 5 | 11.3 | 5.9 | 0 | 4.4 | 13.7 | 17.7 | 14.9 | 13.7 | 14.3 |
| | 10 | 12.3 | 5.4 | 2.7 | 0 | 4.9 | 13.3 | 7.4 | 5.6 | 4.9 |
| | 20 | 6 | 16.2 | 28.9 | 27.9 | 3.1 | 6.7 | 16.5 | 29.1 | 28.1 |
| | 40 | 22.1 | 36.1 | 54.3 | 55.9 | 3.9 | 22.4 | 36.3 | 54.4 | 56 |
| | 80 | 21.5 | 37.7 | 59.5 | 64.2 | 18 | 28.1 | 41.8 | 62.2 | 66.7 |
| TFC-SR3 | 1 | 0 | 2.3 | 5.6 | 158 | 3.1 | 3.1 | 3.9 | 6.4 | 158 |
| | 2 | 0.8 | 0 | 5.5 | 156.4 | 8.9 | 9 | 8.9 | 10.5 | 156.7 |
| | 5 | 6.8 | 2 | 0 | 141.7 | 18.8 | 20 | 18.9 | 18.8 | 142.9 |
| | 10 | 61.5 | 58.2 | 58.4 | 0 | 46.8 | 77.3 | 74.7 | 74.9 | 46.8 |
| | 20 | 85 | 83.2 | 83.7 | 60.9 | 42.8 | 95.1 | 93.5 | 94 | 74.4 |
| | 40 | 95.9 | 95.2 | 95.5 | 89.2 | 44.9 | 105.9 | 105.3 | 105.5 | 99.8 |
| | 80 | 98.8 | 98.6 | 98.7 | 96.9 | 36.7 | 105.4 | 105.2 | 105.3 | 103.6 |

Table S5:

| | | Percentage Error (%) | | | | Relative SE Rq | Cumulative Error (%) | | | |
|---|---|---|---|---|---|---|---|---|---|---|
| | $L_0$ (µm) | 1 | 2 | 5 | 10 | | 1 | 2 | 5 | 10 |
| NF270 | 1 | 0 | 4.2 | 2.6 | 8.2 | 13.9 | 13.9 | 14.5 | 14.2 | 16.1 |
| | 2 | 3.2 | 0 | 8.3 | 12.8 | 12.8 | 13.2 | 12.8 | 15.2 | 18.1 |
| | 5 | 9.5 | 11.7 | 0 | 3.9 | 8 | 12.4 | 14.2 | 8 | 8.9 |
| | 10 | 16.2 | 17.5 | 3.3 | 0 | 9.2 | 18.6 | 19.8 | 9.8 | 9.2 |
| | 20 | 38.8 | 38.6 | 47.1 | 48.3 | 64.2 | 75 | 75 | 79.6 | 80.4 |
| | 40 | 45.2 | 45.6 | 53.9 | 54.7 | 64.5 | 78.8 | 79 | 84.1 | 84.6 |
| | 80 | 62.3 | 62.9 | 69.2 | 69.4 | 38.9 | 73.5 | 74 | 79.4 | 79.6 |
| BW30 | 1 | 0 | 1.5 | 6.7 | 15.4 | 11.2 | 11.2 | 11.3 | 13 | 19 |
| | 2 | 5.3 | 0 | 7 | 16.3 | 9.1 | 10.5 | 9.1 | 11.4 | 18.7 |
| | 5 | 21.5 | 10 | 0 | 10.9 | 10.7 | 24 | 14.7 | 10.7 | 15.3 |
| | 10 | 45.1 | 26.7 | 13.1 | 0 | 13.1 | 46.9 | 29.8 | 18.5 | 13.1 |
| | 20 | 87.2 | 57.8 | 38.3 | 21.4 | 13.1 | 88.2 | 59.3 | 40.5 | 25.1 |
| | 40 | 116.3 | 75.8 | 51.4 | 31.8 | 16.2 | 117.4 | 77.6 | 53.9 | 35.7 |
| | 80 | 129.5 | 80 | 52.2 | 31.5 | 18.6 | 130.8 | 82.1 | 55.5 | 36.6 |
| NF90 | 1 | 0 | 36.9 | 45.7 | 46.1 | 7.7 | 7.7 | 37.7 | 46.3 | 46.8 |
| | 2 | 20.1 | 0 | 4 | 3.6 | 9.5 | 22.3 | 9.5 | 10.3 | 10.1 |
| | 5 | 11 | 1 | 0 | 1.4 | 13.7 | 17.6 | 13.7 | 13.7 | 13.7 |
| | 10 | 1.6 | 3.4 | 2.1 | 0 | 4.9 | 5.2 | 6 | 5.4 | 4.9 |
| | 20 | 41.8 | 32 | 27.5 | 24 | 3.1 | 41.9 | 32.2 | 27.7 | 24.2 |
| | 40 | 88.7 | 60.7 | 51.8 | 46.5 | 3.9 | 88.8 | 60.8 | 51.9 | 46.6 |
| | 80 | 117 | 69 | 56.1 | 49.5 | 18 | 118.4 | 71.3 | 58.9 | 52.7 |
| TFC-SR3 | 1 | 0 | 2.3 | 35.3 | 66 | 3.1 | 3.1 | 3.9 | 35.4 | 66 |
| | 2 | 2.1 | 0 | 20.2 | 88.4 | 8.9 | 9.2 | 8.9 | 22.1 | 88.8 |
| | 5 | 0.3 | 2 | 0 | 111.6 | 18.8 | 18.8 | 18.9 | 18.8 | 113.2 |
| | 10 | 57.6 | 58.2 | 48.7 | 0 | 46.8 | 74.2 | 74.7 | 67.5 | 46.8 |
| | 20 | 83 | 83.2 | 75.1 | 55.4 | 42.8 | 93.4 | 93.5 | 86.4 | 70 |
| | 40 | 95.2 | 95.2 | 91.4 | 85.9 | 44.9 | 105.2 | 105.3 | 101.9 | 96.9 |
| | 80 | 98.6 | 98.6 | 97 | 95.4 | 36.7 | 105.2 | 105.2 | 103.7 | 102.2 |